Accepted Manuscript

Geological Society, London, Special Publications

Petrology of the 2020-21 effusive to explosive eruption of La Soufrière volcano, St Vincent: Insights into plumbing system architecture and magma assembly mechanism

Gregor Weber, Jon Blundy, Jenni Barclay, David M. Pyle, Paul Cole, Holli Frey, Matthew Manon, Bridie V. Davies & Katharine Cashman

DOI: https://doi.org/10.1144/SP539-2022-177

To access the most recent version of this article, please click the DOI URL in the line above. When citing this article please include the above DOI.

Received 31 May 2022
Revised 24 February 2023
Accepted 3 March 2023

Supplementary material at https://doi.org/10.6084/m9.figshare.c.6484877

Petrology of the 2020-21 effusive to explosive eruption of La Soufrière volcano, St Vincent: Insights into plumbing system architecture and magma assembly mechanism

Gregor Weber[1*], Jon Blundy[1], Jenni Barclay[2], David M. Pyle[1], Paul Cole[3], Holli Frey[4], Matthew Manon[4], Bridie V. Davies[2], Katharine Cashman[5]

[1]Department of Earth Sciences, University of Oxford, OX1 3AN Oxford, United Kingdom

[2]School of Environmental Sciences, University of East Anglia, NR4 7TJ Norwich, United Kingdom

[3]School of Geography, Earth and Environmental Sciences, University of Plymouth, PL4 8AA Plymouth, United Kingdom

[4]Geoscience Department, Union College, NY 12308 Schenectady, United States

[5]School of Earth Sciences, University of Bristol, BS8 1RJ Bristol, United Kingdom

* Corresponding author (gregor_weber@gmx.de)

Abstract

The 2020-21 eruption of La Soufrière, St Vincent began with extrusion of a viscous lava dome, which was destroyed upon transition to a major explosive phase. Here we present petrological data to reconstruct the processes leading up to these events. Bulk-rock SiO_2 contents range from 52.8 to 55.4 wt. %, classifying the lava and the subsequent scoria as basaltic andesite, the latter being slightly more mafic. Macrocrystal chemistry and modes (plag-cpx-opx-tmt-ol) and crystallinity (45-50 vol. %) are largely identical for both phases of the eruption. Pyroxenes are homogenous and precipitated mostly from andesitic melts. Conversely, plagioclase shows strong normal zonation resulting from magma ascent and stalling at multiple crustal levels. Clinopyroxene thermobarometry reveals that crystallisation predominantly took place between 8 and 13 km depth at temperatures of 997^{+18}_{-35} °C. A lack of evidence for mafic recharge and changes in volatile content and the omnipresence of xenoliths, suggests pre-eruptive destabilisation of an andesitic-dacitic melt pocket that disrupted and entrained antecedent mush. Olivine diffusion profiles show that this interaction preceded the onset of eruption. Low dissolved sulfur contents (≤270 ppm S) place constraints on the total SO_2 gas release. Melt-mush disruption appears to be a dominant driver of eruptions at La Soufrière.

Keywords

Volcano petrology, Thermobarometry, Diffusion, St Vincent, Eastern Caribbean Volcanic Arc

After more than 40 years of dormancy, La Soufrière volcano on the island of St Vincent, Eastern Caribbean, started erupting on 27th of December 2020 (Fig. 1). The eruption commenced with extrusion of a highly viscous lava dome onto the floor of the main crater, adjacent to the lava dome that had been emplaced in 1979. Over the next three months, lava formed an elongated coulee within the crater with a total volume of ~18 x 10^6 m^3 (Joseph et al. 2022; Stinton et al., this volume). The eruption entered a new phase of activity on the 9th of April 2021, when it produced a series of explosive eruptions that generated both tephra-fall and pyroclastic density currents (Cole et al., this volume). The timely evacuation of about 16,000 people (Joseph et al., 2022) was a great success, especially in the context of the 1902/03 eruption of La Soufrière St Vincent that caused the tragic death of more than 1500 people (Pyle *et al.* 2018).

Renewed activity of La Soufrière provides the opportunity to use petrological indicators to investigate the structure and dynamics of the subvolcanic magma feeding system, its controls on the observed activity, and its relation to previous activity. Mobilisation processes of magma from storage zones in the Earth's crust have been reconstructed at numerous arc volcanoes. Many studies have used mineral chemistry and textures to link the input of fresh magma pulses into pre-existing reservoirs (i.e. crystal mushes) to eruption initiation (e. g. Tepley *et al.* 2000; Humphreys *et al.* 2006; Ruprecht and Wörner 2007; Andrews *et al.* 2008; Kent *et al.* 2010; Druitt *et al.* 2012; Bouvet de Maisonneuve *et al.* 2015; Wanke *et al.* 2019; Weber *et al.* 2020). Yet, examples without clear evidence for a relationship between magma recharge and eruption triggering are not uncommon; in such cases, exsolution of dissolved volatiles is frequently invoked in the mobilisation of resident magmas (e. g. Blake 1984; Kent *et al.* 2007; Cassidy *et al.* 2016; Stock *et al.* 2016; Budd *et al.* 2017; Andersen *et al.* 2018; Caricchi *et al.* 2018). External forcing of magmatic systems, for example by large earthquakes, may also contribute towards destabilisation of magma feeding systems and initiation of volcanic eruptions (e.g. Walter and Amelung 2007; Bebbington and Marzocchi 2011; Nishimura 2017; Watt 2019; Seropian *et al.* 2021). Moreover, while some volcanoes show persistent evidence for specific reactivation processes such as mafic magma recharge (e.g. Nevado de Toluca: Weber et al., 2020; Mount Hood: Kent et al., 2010), it is common for both the depth from which magma ascends and the types of mobilisation processes to vary. This can be observed even during different phases of the same eruption or different events at the same volcano (e. g. changes in reservoir depth at Parinacota: Ginibre and Wörner 2007; vapor phase accumulation vs. silicic magma recharge at Mt. St Helens: Kent *et al.* 2007; Cashman and Blundy 2013). It is therefore important to reconstruct magma storage and mobilisation conditions for individual eruptions to link specific

petrological processes to geophysical monitoring signals, which can in turn provide valuable insights for future volcanic hazard mitigation.

Based on analysis of earlier eruptive products, current petrological models of the magmatic plumbing system beneath La Soufrière consider it to be characterised by a vertically extensive and compositionally diverse plexus of storage zones (Fedele *et al.* 2021). The recent eruptions of La Soufrière, St Vincent provide an excellent opportunity to compare mineralogically derived pressure estimates with observed depths of unrest and activity recorded by contemporaneous geophysical detection and related surface activity. Pressure and temperature reconstructions employing mineral-melt equilibria are challenging at La Soufrière due to the high crystallinity and groundmass microlite content of the erupted products. However, such estimates are required to constrain the depths from which magma was sourced, to understand the reactivation process that primed the feeding system for eruption and to explain why La Soufrière eruptions often switch between explosive and effusive phases (Robertson, 1995).

Here we present detailed petrography and mineral chemistry from the now destroyed 2020-21 lava dome and subsequent explosive phase of the 2020-21 eruption of La Soufrière St Vincent. We use a petrological modelling approach based on melt inclusion chemistry to reconstruct a wide range of magma system variables. Based on these data, we propose a conceptual model of the magma feeding system and mobilisation processes for the 2020-21 eruption that we compare with the geophysical indicators of melt movement and degassing obtained during the course of the eruption. This paper complements that of Frey et al. (this volume), which focusses on the evolving compositions and textures of microlites and their relative abundances during the effusive and explosive sequence.

Volcanic geology and petrology of La Soufrière St. Vincent

La Soufrière St Vincent (13° 20′ 20″ N, 61° 10′ 43″ W) is one of the most active and hazardous stratovolcanoes in the Eastern Caribbean (Robertson 1995). Located in the southern part of the Eastern Caribbean Volcanic Arc, it is part of an 800 km-long chain of subaerial and submarine volcanoes fuelled by hydrous basaltic melt produced in response to westward subduction of the North and South American plates beneath the Caribbean plate (Macdonald *et al.* 2000; Cooper *et al.* 2020). Throughout its history, La Soufrière has produced basalts and basaltic andesites of monotonous transitional calc-alkaline to tholeiitic affinity (Heath *et al.* 1998a). While the eruptive products are restricted in geochemistry, the volcano exhibits a range of eruptive styles that includes lava flows and domes as well as explosive paroxysms that often feature pyroclastic density currents and lahars (Robertson 1995; Cole *et al.* 2019). In historic time, La Soufrière has produced at least

four explosive eruptions (Cole *et al.* 2019), including a large paroxysm in 1902/1903 classified as a Volcanic Explosivity Index (VEI) of 4 (Pyle *et al.* 2018). Between 1903 and the 2020-21 eruption, the volcano had two eruptive episodes: a purely effusive event in 1971-72 that produced a lava dome in the water-filled central crater (Aspinall *et al.* 1973) and a series of explosions in 1979 followed by the extrusion of a large lava dome (Shepherd *et al.* 1979; Fiske and Sigurdsson 1982; Graham and Thirlwall 1981).

Since the 1980s, petrological, experimental, geochemical, and isotopic studies have been used to develop conceptual models of the structure and dynamics of the igneous plumbing system beneath St. Vincent. The generation of primary basaltic melts, in particular, has received much attention through petrological experiments (Pichavant *et al.* 2002; Pichavant and Macdonald 2007; Melekhova *et al.* 2015, 2019), whole-rock and mineral chemistry (Heath *et al.* 1998a), and melt inclusions studies (Bouvier *et al.* 2008, 2010). High-MgO basalts from St. Vincent are found to represent primary mantle melts generated by partial melting of a MORB-like lherzolitic mantle source previously metasomatized by slab-derived fluids (McDade *et al.* 2003). The last equilibration conditions of these basalts with their mantle source lie between 11.5 and 16 kbar and 1185 to 1235°C under relatively oxidizing conditions above the quartz-fayalite-magnetite buffer (QFM+1 – QFM+2 log units) and with water contents of 1.5 to 4.5 wt.% (Heath *et al.* 1998b; Pichavant *et al.* 2002; Pichavant and Macdonald 2007). Using primitive melt inclusions containing 1.5 to 4 wt.% H_2O, Bouvier *et al.* (2008, 2010) argued for a slightly more restricted (but consistent) range of mantle melting conditions, 13-14.5 kbar and 1220-1190°C.

Basaltic andesites from La Soufrière show mantle-like isotopic signatures, consistent with an interpretation that crustal melting does not play a major role in the petrogenesis of rocks at St Vincent (Heath *et al.* 1998a; Graham and Thirlwall 1981; Tollan *et al.* 2012). Eruptive products are typically highly porphyritic; phase equilibria considerations suggest that basaltic andesites are derived from high-MgO basalt parents through fractional crystallisation at pressures of 7 to 10 kbar and temperatures between 1050 and 1130°C (Heath *et al.* 1998a; Melekhova *et al.* 2015). Trace element data show, however, that basaltic andesites from recent eruptions (1971, 1979) may not represent simple derivatives of each other, but instead derive from separate magma batches (Graham and Thirlwall 1981). Further inferences on magma differentiation processes have been drawn from detailed studies of coarse-grained 'plutonic' gabbroic to ultramafic xenoliths, which are ubiquitous in La Soufrière magmas (Wager 1962; Arculus and Wills 1980; Tollan *et al.* 2012; Melekhova *et al.* 2015, 2019).

Insight into eruptive processes comes from crustal residence times of basaltic andesite magma batches of tens of thousands of years as determined from U-Th disequilibria (Heath *et al.* 1998b). Comparison of published experimental data and SEM-EDS mineral compositions from the historic and prehistoric (pre-1700 AD) activity of La Soufrière suggests that eruptions are initiated at shallow crustal levels (~1-4 kbar) by volatile accumulation pressure but may also involve episodic rejuvenation of shallow crustal basaltic andesite intrusions with more mafic magma (Fedele *et al.;* 2021). Diffusion modelling of Sr concentrations in plagioclase crystals, indicates shallow magma residence times of about 150 years (Zellmer *et al.* 1999).

In summary, previous constraints based on petrological experiments on the subvolcanic plumbing system of St Vincent indicate deep generation of primitive basaltic magmas in the mantle at 11-16 kbar and 1185 to 1235°C. These parental magmas ascend and fractionate to produce basaltic andesite at ~7-10 kbar and temperatures of 1050-1130°C, before being stored and erupted from shallow (1-4 kbar) crustal levels. Plutonic xenoliths capture snapshots of this process throughout the crust (Melekhova et al., 2019). In this study we provide the first detailed mineral-melt thermobarometry for La Soufrière St Vincent to better constrain the magma source depth and evaluate eruption initiation processes and timescales prior to the 2020-21 eruption.

Materials and Methods

Studied samples

The samples analysed in this study were collected during two field campaigns in January and April 2021, targeting the effusive and explosive phases of the eruption respectively. A sample of the 2021 lava dome collected on an active lobe of the advancing flow on the 16th of January 2021 (13°20'1.71" N, 61°11'10.36" W) was split into 8 subsamples. This represented a discrete sub-sample of one part of the dome at a relatively early stage of its growth. Importantly, because of safety and logistical concerns, spatial and temporal heterogeneity could not be assessed. Juvenile scoria samples were collected from the upper parts of the April pyroclastic deposit, where clasts were largest. These clasts represent scoria generated during the later explosions of the sequence and were sampled in three separate locations in the East and Northeast of the island. We analyse 14 samples of the explosive phase that were very likely erupted on 10th/11th April 2021. These samples are from clasts sampled in April and May 2021 at five locations around the volcano, representing later phases of the explosive eruptions (U3 to U7 Cole et al., this volume). The PDC clast samples were quenched on sampling so assumed to represent fragmented magma incorporated into the PDC. The

sampled materials and locations, GPS coordinates and performed analyses are listed in supplementary table 1.

Analytical methods

Microscopic imaging

Five petrographic thin sections of the 2021 lava dome sample, three of the late-stage scoria (U3 and U5 unit; supplementary table 1), were examined using polarized light microscopy. To establish the proportions of individual phases, we obtained full photographic scans of all thin sections in plane and crossed polarized light. Modal percentages were determined on the scans by random grid-point counting using the software package *JMicroVision* version 1.3.1 (Roduit 2007). To establish robust modal percentages, a grid of random locations (points) was allocated on each thin section. For each random point, the phase was identified and counted until the phase proportions converged to constant values, which was readily achieved with more than 500 counted points. All modal percentages were calculated on a vesicle free basis, which required high resolution back-scatter electron imaging (BSE) to resolve scoria micro-vesicularities. Back-scatter electron images were collected using a JEOL JXA-8200 electron microprobe at the Research Laboratory for Archaeology and History of Art, University of Oxford.

Bulk-rock analysis

The major and minor element compositions of selected bulk-rock samples were determined by x-ray fluorescence analysis (XRF) at the University of Plymouth (UK) and by inductively coupled plasma optical emission spectrometry (ICP-OES) at AcmeLabs, a division within Bureau Veritas (US). For the whole-rock major element chemical analyses by ICP-OES, powdered samples were prepared with a lithium borate flux followed by a highly aggressive dissolution. Detection limits of these analyses are <0.01% for most oxides. For XRF analysis, samples were mixed with lithium tetraborate and lithium metaborate flux and converted to glass beads. Measurements were carried out using a Panalytical Axios Max instrument.

Electron microprobe analysis

The major and minor element composition of crystals was determined at University of Oxford by electron probe microanalysis (EPMA), using a JEOL JXA-8200 at the Research Laboratory for Archaeology and History of Art and a Cameca SX-5 FE in the Department of Earth Sciences. Mineral analyses were obtained with a focussed beam, 15 kV acceleration voltage and 15-20 nA beam current. Primary calibration was carried out on in-house standards: Albite (Na, Si, Al), Sanidine (K), TiO_2 (Ti), elemental Mn, Cr and Ni, and Andradite (Fe, Ca). Peak counting times for mineral analysis

were as follows: 20 s for Na; 30 s for Mg, Si, Al, K, Fe, Ca; and 40 s Ti, Mn Cr, Ni. A subset of plagioclase analyses was carried out with increased beam current of 40 nA and peak counting times of 180 s to measure TiO_2 contents. Silicate mineral analyses that returned analytical totals outside the range 98.5 to 101.5 % were discarded. At the beginning and end of each analytical session, we measured several secondary standards for quality control (supplementary table S10).

The bulk microlite-rich groundmass of scoria samples was analysed in 22 randomly distributed spots with a 20 µm defocussed beam, 15 kV acceleration voltage and beam current of 10 nA. To mitigate diffusive alkali loss during analysis, Na and K measurements were placed first in the sequence with reduced peak counting times of 15 s and 20 s respectively. Peak counting times for all other elements were 30 s. Analytical totals for interstitial groundmass analyses ranged between 98.6 to 99.9 % indicative of low dissolved volatile contents.

Melt inclusions hosted in plagioclase and pyroxene crystals from the explosive phase of the eruption were analysed by EPMA using a JEOL JXA-8350 F in the School of Earth Sciences at the University of Bristol. Analysis conditions included a 5 nA beam current, a 10 µm spot size and an accelerating voltage of 15 kV; K, Ca, Si, Na, and Al were analysed first for 10 s, Ti and Mg for 60 s and Fe, Mn, P, S, and Cl for 50 s. Barite was used as calibration standard for S measurements. Water contents were estimated using an iterative method for obtaining volatiles by difference (in Probe for Windows; see Roman *et al.* 2006). This method corrects matrix effects that can arise in the presence of H_2O in glasses by iteratively adjusting water contents and recalculating the glass composition. Typical uncertainty of the method is less than 0.5 wt.% (Roman *et al.* 2006).

Results

Petrography

Polarized light and back-scatter electron images show great similarity in textures and mineralogy between the 2020-21 lava dome and scoria samples (Fig. 2). Both lava and scoria samples are characterised by a high crystal content (45±1.9 vol. %; 1 standard deviation) and a mean mode of plagioclase (26.1±1.9 %), orthopyroxene (8.1±1 %), clinopyroxene (5.9 ±1.7 %), titanomagnetite (4.5±1.1 %), and olivine (0.6±0.4 - 2.2±0.5 %) (Fig. 2a, b; Fig. 3). Given the variation between the different thin sections counted (dome: n=5, scoria: n=5; Fig. 3; Supplementary table SM2), crystallinity and macrocrystal modes for the dome and scoria samples analysed in this study are not distinct except for olivine, which is more abundant in the scoria. Noticeable differences also exist in olivine textures, which show reaction coronas comprised of orthopyroxene and Fe-Ti oxides in lava dome samples (Fig. 2a) compared with their more pristine but subhedral embayed appearance in

scoria samples (Fig. 2b). Plagioclase crystals record strong normal zonation pattern in BSE images, in some cases weak oscillatory zoning, and generally euhedral crystal habits (Fig. 2c-e). Pyroxene crystals from the explosive phase of the eruption appear to be in textural equilibrium, with most grains showing facetted crystal faces and appearing compositionally homogeneous in BSE images. Similarly, pyroxenes in the lava dome are mostly euhedral but often show feathery reaction textures on crystal rims (Fig. S1c). Titanomagnetites frequently occur as inclusions in pyroxenes, are sub- to euhedral in shape, and show exsolution textures in lava dome samples but are homogeneous in samples from the explosive phase of the eruption.

Similar to historic eruptions (Fedele et al. 2021), plutonic xenoliths are abundant in the studied explosive samples, spanning a size range from centimetres to the sub-millimetre scale (Fig. 4). We distinguish two types of xenoliths based on their mineralogy and textures: 1) Troctolite xenoliths comprise unzoned plag-ol assemblages with minor titanomagnetite and some interstitial vesicularity (Fig. 4a). 2) Gabbronorite xenoliths (plag-opx-cpx-tmt±ol) feature poikilitic titanomagnetite in pyroxenes, olivine rimmed by orthopyroxene reaction coronas, and strongly zoned plagioclase (Fig. 4b-d). Both xenolith types are hosted in the groundmass without chilled margins. All major phases also occur as glomerocrysts of highly variable modal mineralogy with strong resemblance in plagioclase zonation pattern to free-floating macrocrystals.

In both eruptive phases the groundmass has a hyalopilitic (microlite-rich) texture comprised of plagioclase, clinopyroxene, orthopyroxene, titanomagnetite and sparse olivine microlites with small (<10 µm) pockets of interstitial glass. The microlite population in the lava dome shows abundant reaction textures, whilst appearing pristine in explosive samples. Both eruptive phases have plagioclase crystals in the groundmass that can be subdivided into unzoned microlites (<30 µm in length) and strongly zoned microphenocrysts (>30 µm). A detailed petrological and textural analysis of the microlites reveals distinct variations of groundmass phase proportions in stratigraphically constrained samples (Frey et al., this volume). As shown by Frey et al. and Morrison-Evans et al. (this volume), reaction textures in dome samples typically comprise <1µm Fe-Ti oxide halos surrounding orthopyroxene crystals, symplectite textures in rare olivine macrocrysts and exsolution textures in Fe-Ti oxide macrocrystals. Further difference in the microlite population of dome and scoria samples are the greater abundance of orthopyroxene microlites in the lava dome and the presence of olivine microlites exclusively in explosive samples (Frey et al., this volume).

Bulk-rock geochemistry

All analysed bulk-rock samples (n=26) classify as basaltic andesite with SiO_2 contents ranging from 52.8 to 55.4 wt.% (Fig. 5). Scoria samples of the explosive phase (n=18) are slightly more mafic with

mean SiO_2 contents of 54.6 wt.% (±0.6 1SD) compared to dome samples (n=8) whose mean SiO_2 is 55.2 wt.% (±0.1 1SD). Bulk-rock data follow a linear trend in total alkalis versus silica space and in components such as MgO and CaO, consistent with the trajectories defined by historic eruptions of La Soufrière (Fedele *et al.* 2021). Based on available data (Fedele *et al.* 2021), whole-rock compositions of the 2020-21 eruption are on average slightly more mafic than samples from historic (1718/1812AD; SiO_2 wt.% range: 53.6 - 56.2) and prehistoric (1440AD: 55.3 - 56.2 SiO_2 wt.%; 1580AD: 54.2 - 56.5 SiO_2 wt.%) eruptions, but do not extend to such mafic compositions as the 1902/1903 eruption (50.1 -55.5 wt. % SiO_2). Overall, lava dome samples from the 2020-21 eruption are slightly more silicic than the 1979 dome and scoria (SiO_2 wt.% range: 54 - 55). The scatter in the 2021 scoria data is most likely related to different amounts of entrained xenolith material that contribute to the bulk-rock composition.

Mineral and glass chemistry

Plagioclase

Plagioclase (n = 373 spot analyses from 52 crystals) shows a wide range of compositions with molar percentage anorthite (An; $CaAl_2Si_2O_8$) ranging from 48 to 96% and FeO_t contents varying between 0.42 and 0.98 wt. % (Fig. 6). Crystals from lava dome and scoria samples are chemically indistinguishable (Fig. 6a). Most crystal cores define a slightly inverse sloping trend from An_{80} to An_{95} in An-FeO_t space with considerable variation in FeO_t contents between 0.4 and 0.9 wt. % (Fig. 6b). Plagioclase macrocryst rims cluster around a median of An_{61} and FeO_t of 0.56 wt. %. The strong bimodality of high An plagioclase core and lower An rim compositions produces distinctive abrupt changes in BSE greyscale intensity (Fig. 2e, g). Microlites (<30 µm) are distinct from macrocrystal rims, with elevated FeO_t contents (0.78-0.98 wt.%) and median of An_{52}. A broader range of FeO_t contents in plagioclase between 0.6-1.6 wt.% was reported by Frey et al. (this volume), but the majority of their analyses are consistent with the range reported here. The outermost microphenocryst rim compositions are similar in An to microlites but typically lower in FeO_t; An_{70}-An_{91} cores of microphenocrysts have 0.60-0.88 wt.% FeO_t. Xenolith and glomerocryst plagioclase crystals have compositions of An_{60}-An_{94} and FeO_t = 0–.49 - 0.92 wt.%.

Pyroxenes

Orthopyroxene (opx) and clinopyroxene (cpx) macrocrystal cores and rims have a restricted range in major element composition (Fig. 7). Enstatite (En; $Mg_2Si_2O_6$) contents in cpx (n=240 spot analyses) range from En_{37}-En_{45} (Mg# 65-78) with a median of En_{42}, whereas opx (n=321 spot analyses) compositions vary between En_{61} and En_{73} (Mg# 64-75) with a median of En_{66}. Al_2O_3 varies between 0.6 to 5.8 wt. % (median: 1.9 wt. %) in cpx and –.5 - 2.2 wt.% (median: 1.1 wt. %) in opx and is

correlated with TiO_2 contents, which are 0.3-1.3 wt.% (median = 0.5 wt.%) in cpx and 0.2-0.5 wt.% (median: 0.3 wt.%) in opx. Cpx Na_2O shows little variation around a median of 0.3 wt.%. There is no compositional difference in pyroxenes from lava dome and scoria samples (Fig. 7a). Furthermore, outermost rim and core compositions, as well as different crystal types (i. e. macrocysts, glomerocrysts, plutonic xenoliths) are similar in dome and scoria samples, except that microlite compositions span a larger compositional range (En_{37} to En_{72}; Mg# 59-78) (Fig. 7b, c). Frey et al. (this volume) report a similar microlite opx Mg# range of 59-74 and a Mg# of 67-89 in cpx microlites.

Olivine

Forsterite (Fo; Mg_2SiO_4) contents in olivine phenocrysts (n=193 analyses) range from 62 to 82 mol. % and show a bimodal distribution with average values of Fo_{76} and Fo_{63} for the two groups. Most analyses (88 %) belong to the high Fo cluster (Fo_{72}-Fo_{82}), corresponding the bulk interior of most olivine crystals. Scare symplectic olivine grains in the dome lava (n=7 analyses) record Fo contents between 74 and 82 mol.%. Texturally, high Fo cores are found in scoria olivine macrocrysts and in xenolith grains that have not been in direct contact with the carrier melt (Fig. 8). Crystal rims (both macrocrysts and xenolith grains) that have been exposed to the carrier melt have outermost rim Fo contents of 66 to 77 mol.%, likely reflecting varying extents of diffusive re-equilibration with the melt. Two analysed remnant olivine cores surrounded by coronas of peritectic orthopyroxene have relatively constant and evolved compositions of Fo_{65} and Fo_{62}, respectively. MnO (wt.%) is negatively correlated with Fo, with higher MnO values (0–59 - 0.83 wt.%) in the low Fo group and lower values (0.30 and 0.58 wt. %) in the high Fo group. CaO contents of 0.10 – 0.26 wt. % are indistinguishable between low and high Fo groups. Olivine crystals in xenolith interiors, remote from the carrier melt, are compositionally homogeneous ($Fo_{76\text{-}77}$). No melt inclusions were observed in the studied olivine crystals.

Oxides

Fe-Ti oxides (n=177 analyses) classify as titanomagnetites and have a restricted compositional range in scoria samples, with ulvöspinel (Fe_2TiO_4) molar fractions of 0.37 to 0.41. An exception is a single grain hosted in a xenolith with an MgO content (3.43±0.25 wt.%) that is slightly higher than the average of 3.27±0.14 wt.%. No significant variation was observed between crystal cores and rims. While Fe-Ti oxides in the explosively erupted samples are homogeneous, lava dome samples show exsolution lamellae of Ti-rich compositions hosted in Fe-rich grains (supplementary Fig. S1; Morrison-Evans et al. this volume). No discrete ilmenite grains were found in any of the samples.

Interstitial glass and melt inclusions

Groundmass glasses (n=10 spot analyses), interstitial between microlites, were only analysed in the lava dome sample as sufficiently large glass patches (>10 μm) were not found in the scoria samples. Lava dome interstitial glasses are rhyolitic in composition, ranging in SiO_2 from 70.80 – 78.61 wt.% (median: 77.97 wt.%). Frey et al. (this volume) describe more mafic (andesitic-dacitic) interstitial glasses in the scoria. Melt inclusions (n=18) were analysed only in rapidly quenched scoria samples, hosted in plagioclase and pyroxene crystals. The inclusions show rounded morphologies, were glassy and devoid of bubbles. The analysed inclusions are andesitic to dacitic in composition (58.66-67.20 wt.% SiO_2) with median SiO_2 of 64.06 wt.%. No compositional difference is observed between plagioclase and pyroxene hosted inclusions.

Magmatic system variables

Volatile contents

The concentration of pre-eruptive magmatic volatile species (H_2O, Cl, S) was constrained by EPMA analysis of melt inclusions (n=18) hosted in plagioclase and pyroxene crystals from the explosive phase of the eruption (Supplementary table 8b). Water contents, calculated using an iterative approach to the volatiles by difference method with typical uncertainty of less than 0.5 wt.% (Roman *et al.* 2006), range from 1.5 to 3.9 wt.% H_2O, which is similar to but slightly lower than previously published melt inclusion data for more primitive St. Vincent magmas (0.8 to 5.2 wt.% H_2O ; Bouvier et al. 2008). Cl contents range from 0.21 to 0.28 wt.% and show a weak tendency towards increasing values with decreasing water content (R^2=0.32). No correlation is evident for Cl or H_2O contents with S in melt inclusions, which range from 44 to 266 ppm, although these low S concentrations have large errors when measured by EPMA (average ~ 60%).

Composition of the carrier melt

The composition of the carrier melt in which macrocrystals are embedded is difficult to measure directly because of the high groundmass crystallinity. For this reason, the carrier melt composition, here defined as groundmass glass + microlites, must be reconstructed using different methods. Given that these reconstruction methods have strengths and limitations that may impact thermobarometric estimates, we propagate the uncertainty resulting from different approaches using a threefold strategy to determine the carrier melt chemistry: 1) Mass balance calculations based on phase proportions, bulk-rock and mineral chemistry (described in the supplementary materials); 2) averaging of bulk groundmass composition as determined by 22 defocussed beam analysis; and 3) pyroxene-hosted melt inclusion analysis.

As we demonstrate below, all reconstructed permissible carrier melt compositions indicate that the crystal cargo of the 2020-21 eruption was brought to the surface in an andesitic to dacitic melt during both the effusive and explosive eruptive phases (Fig. 9; Table S8a-c). Importantly, all reconstructed carrier melt compositions are consistent with the melt evolution trend defined by published melt inclusion data for historic eruptions from La Soufrière. Melt compositions for five thin sections reconstructed by mass balance give broadly consistent results for all major element oxides with SiO_2 contents of 61.3 – 63.0 wt. % for the 2020-21 lava dome and slightly more mafic chemistry (59.6 – 61.1 wt. % SiO_2) for scoria samples. Melt inclusions from the 2020-21 scoria record slightly more silicic melt compositions (58.7 to 67.2 wt. % SiO_2; average = 63.8 wt.%) but may have been modified by post-entrapment crystallisation, as there is considerable scatter in the data. Alternatively, they may represent melt trapped at previous evolutionary stages resulting from crystallisation processes rather than carrier melt itself (Kilgour et al. 2013). Groundmass analyses with a defocussed beam are slightly lower compared to melt inclusions (average 62.0 wt. % SiO_2) with a range of 59.3 to 64.3 wt. % SiO_2 resulting from scatter of individual defocused beam analyses. The range of estimates for the scoria samples relates in part to the spread in bulk-rock compositions, where higher olivine contents derived from plutonic xenoliths may shift the reconstructed melt to more mafic compositions. Given the differences in sample size, we average the results of each reconstruction approach independently. This suggests that the carrier melt of the 2020-21 eruption was andesitic to dacitic in composition with silica contents of 60 to 64 wt. %.

Clinopyroxene-liquid equilibria and thermobarometry

Reliable temperature and pressure reconstructions based on cpx chemistry require knowledge of the melt composition in equilibrium with the crystals, which is not known *a priori*. The restricted range of cpx major and minor element variation indicates, however, that the crystals have grown from mostly similar melts that may be represented, as a first approximation, by either the bulk-rock or the range of estimated andesitic to dacitic carrier melts (Fig. 9a). Without further testing, however, it cannot be presumed that either the bulk-rock or the groundmass composition (i.e. carrier melt) represents a plausible equilibrium liquid. To test if equilibrium conditions between the observed cpx compositions and the permissible melts prevailed, we calculated Fe-Mg exchange coefficients (i.e. $K_D^{cpx-liq} Fe-Mg$), which at equilibrium should vary between 0.24 and 0.3 (Putirka 2008). As a further test for equilibrium, we also calculated the mismatch between predicted and observed Diopside-Hedenbergite components in cpx (hereafter called ΔDiHd; Scruggs and Putirka 2018). The predicted DiHd component in cpx was calculated based on cation fractions in the liquid phase following Putirka (1999). Observed DiHd components were calculated using a normative scheme (Putirka *et al.* 1996). To establish whether these two parameters effectively constrain equilibrium

conditions between cpx and melts similar to those erupted from La Soufrière St Vincent, we compared experimental cpx-melt pairs from St Kitts in the northern Lesser Antilles (Melekhova et al., 2019; Fig. 10a, b) with known pressure and temperature conditions to thermobarometric reconstructions using the model of Putirka (2008) (their eqns. 30 and 33). As shown in Fig. 10b, reliable pressure and temperature estimates are retrieved for experimental cpx-liquid pairs that show $K_D^{cpx-liq} Fe-Mg$ in the range 0.24 to 0.3 and ΔDiHd between -0.1 and 0.1, giving confidence that these filtering criteria are suitable to recover reliable pressure and temperature estimates.

Fe-Mg exchange coefficients and ΔDiHd were determined for a range of permissible melt compositions (Fig. 10a), including the median bulk-rock composition of the lava dome and scoria, reconstructed groundmass compositions from defocussed beam analysis (median, 1st and 3rd quartile) and mass balance (5 thin sections for scoria and dome each), as well as the melt inclusion compositions (median, 1st and 3rd quartile). All calculations were performed with a melt $Fe^{2+}/(Fe^{2+} + Fe^{3+})$ ratio of 0.68 to 0.78. This is equivalent to an oxygen fugacity (Gualda *et al.* 2012) of 1 and 2 log units above the quartz-fayalite-magnetite buffer (QFM+1 and QFM+2), consistent with previous estimates for La Soufrière (Heath *et al.* 1998a), and water contents of 3.9 wt.% based on our estimate described above. Using average bulk-rock compositions as liquid yields $K_D^{cpx-liq} Fe-Mg$ variations between 0.4 and 0.5 with only 2% of the cpx-liquid pairs at permissible equilibrium conditions (Fig. 10c). Andesitic to dacitic carrier liquid compositions based on mass balance and defocussed beam analysis yield equilibrium conditions for 23% and 27% of the cpx-liquid pairs, respectively. The overall best fit is observed using melt inclusion compositions (median, 1st and 3rd quartile) as liquid, which results in a 48% match. Note that these percentages incorporate all cpx data (see also supplementary Fig. S4), while Fig. 10c shows a subset for which measurements of distance from crystal rims are available.

The results indicate that only a small number of the clinopyroxenes analysed could have been in equilibrium with a liquid composition equivalent to the basaltic andesite bulk rock. We therefore conclude that the bulk-rock does not sufficiently approximate the melt composition from which most of the cpx crystals formed. Clinopyroxene crystals, in contrast, may have precipitated from a liquid similar to the carrier melt. Andesitic to dacitic liquids as represented by melt inclusion compositions and groundmass analysis cannot explain the full dataset, however, adding uncertainty to pressure and temperature estimates for magma crystallization in the volcanic plumbing system. Given that glass inclusions from historic eruptions of La Soufrière show a well-defined major element oxide melt evolution trend that diverges from the array of whole rock compositions in various components (Fig. 9), potential equilibrium melts may have different compositions to the explored

range. Consequently, we also used a modelling approach to reconstruct the most likely melts in equilibrium with cpx based on the relation provided by the melt inclusion trend. This modelling approach explores a much wider compositional spectrum compared to the reconstructed melts. Major element oxides were expressed as a function of silica content using three exponential models (central, lower, and upper prediction intervals); fits correspond to 50 and 65% prediction levels, to account for variability in the data (red dashed curves in Fig. 9). An exponential rather than linear model was chosen because of curvature in liquid lines of descent, although the scatter in melt inclusion data limits the importance of the choice of exponential over linear fit. Melts were calculated in increments of 1 wt. % between 50 and 70 wt. % SiO_2 and subsequently used to calculate Fe-Mg exchange coefficients and ΔDiHd for all combinations of model melt and cpx analyses. The resulting distribution of $K_D^{cpx-liq}(Fe-Mg)$ and ΔDiHd is shown in Fig. 11a, colour contoured for melt SiO_2, and illustrates the impact of melt chemistry on cpx-liquid equilibria for La Soufrière compositions. Considering all permitted equilibrium pairs of cpx and melt calculated using this approach, a maximum is observed for melt compositions between 55 and 60 wt. % SiO_2 (Fig. 11b). Depending on the model choice, possible equilibrium liquids show a maximum at basaltic andesite (upper model) to andesites equivalent to the carrier melt (lower model; Fig. 11b). From this we conclude that part of the cpx crystal population of the 2020-21 eruption originally precipitated from basaltic andesite liquids that were similar but not identical to the whole rock composition. Equilibrium crystallisation of such basaltic andesite liquids may explain the observed variation in slow diffusing minor elements such as Al_2O_3 in cpx crystals and is consistent with the opx reaction coronas found around xenolith olivines (Fig. 4b-d).

Pressures and temperatures of cpx crystallisation were calculated using matching groundmass and melt inclusion liquids (n=858), as well as the entire range of modelled equilibrium melt-cpx pairs (n=4183), thus incorporating the uncertainty stemming from melt composition. Calculations were performed with 2 to 4 wt. % H_2O in the melt, consistent with melt inclusion data for the 2020-21 eruption and with previous estimates of the water content of St. Vincent magmas (Heath *et al.* 1998a; Bouvier *et al.* 2010). We used three recent thermobarometric models based on either conventional linear regression of high pressures-high temperature experimental data (Putirka 2008; Neave and Putirka 2017) or a machine learning approach that uses an extremely randomized trees algorithm (Petrelli *et al.* 2020). The latter technique predicts pressures and temperatures by generating a large number of hierarchical charts (regression trees) that compare an observed cpx population with experimental data (for details see Petrelli et al., 2020).

Temperatures calculated using groundmass cpx pairs and equation 33a of Putirka (2008) indicate crystallisation conditions of 962±15°C (median±1 sd) compared with the temperature derived from machine-learning thermometry (1015±10°C; Fig. 12a). These results agree with each other within relative mean standard error (RMSE) of 40-60°C (errors resulting from analytical uncertainty are much smaller) for both methods and together yield an average pre-eruptive temperature of 997^{+18}_{-35} °C (median, ±IQR: inter quartile range, 1 sd =29°C). If we use the modelling approach described above to allow for a greater variability of melt compositions through the modelling, we recover a median temperature of 1027±38°C. Cpx crystallisation pressures calculated using Neave and Putirka (2017) range from -5 to 1.5 kbar but recover mostly negative pressures and are therefore not considered further. The barometer of Putirka (2008; eqn. 30) recovers a median pressure of 3.4 kbar with most estimates between 2.8 and 4 kbar (IQR). Pressures calculated using the machine learning algorithm of Petrelli *et al.* (2020) indicate a narrower IQR between 2.5 and 2.9 kbar with most estimates around a median of 2.7 kbar (Fig. 12b). The larger range of the Putirka (2008) barometer likely relates to the greater uncertainty of his method (RMSE of 4.5 kbar) compared to the machine-learning algorithm (RMSE=2.9 kbar). Taken together, these approaches indicate pressures of pyroxene crystallisation ~ 2 to 3 kbar. Considering the full array of possible equilibrium melts expands the range of temperatures in both approaches but recovers similar median pressures and temperatures of 2.6 kbar and 1027°C. No difference is found in thermobarometric reconstructions for cpx from the dome and scoria samples, within the range represented by the variance we observe and the uncertainty of the modelling approach. Model water contents affect the temperature and pressure estimates of the Putirka (2008) model only within a range of ±10°C and ±0.7 kbar for 1 wt.% change in H_2O. The model of Petrelli *et al.* (2020) is not sensitive to water contents. In summary, the clinopyroxene crystal cargo of the 2020-21 eruption of La Soufrière records crystallisation temperatures of around 1000 °C (RMSE ±40°C) and pressures between 2 and 3 kbar, with little textural evidence of significant time to re-equilibrate at different conditions.

Two-pyroxene thermometry

The cpx-opx thermometer of Putirka (2008) was used to test for equilibrium conditions and to calculate crystallisation temperatures (Fig. 13). Reported uncertainty for this calibration is on the order of ±38°C (Putirka, 2008). Calculated temperatures range from 894 to 1023°C with slightly higher temperatures for the scoria samples (median: 969°C) compared to the dome (median: 943°C). However, calculated Fe-Mg exchange coefficients lie mostly outside the accepted range of 1.09±0.14 (Putirka, 2008) for crystallisation under magmatic conditions (grey shaded field in Fig. 13a), instead having low values (median±1sd: 0.86±0.09) more consistent with sub-solidus systems (red shaded

field in Fig. 13a). Low $K_D^{cpx-opx}(Fe-Mg)$ values are observed for random combinations of outermost cpx and opx rims that were in contact with the carrier melt, touching opx-cpx grains in glomerocrysts and xenoliths, as well as directly touching profiles across opx-cpx grain boundaries (Fig. 13b). Given that pyroxene compositions in xenoliths, glomerocrysts and macrocrystals are identical, this does not imply that the grains have grown from a liquid of different composition to the carrier melt but could reflect that the Fe-Mg exchange coefficient of 1.09±0.14 is not applicable in this case. This may reflect uncertainty in the estimated Fe^{3+} of the pyroxenes, which in turn affects $K_D^{cpx-opx}(Fe-Mg)$. Generally, the calculated two-pyroxene temperatures broadly agree with reconstructions based on cpx-liquid thermometry but are not considered further due to the failed equilibrium test.

Plagioclase thermometry

The plagioclase-melt thermometer of Putirka (2005) was used to further constrain pre-eruptive temperatures. Calculations using all plagioclase analyses (rims and cores) and the bulk rock composition of the dome and explosive phase show that, as for cpx, an assumed $K_D^{plag-liq}$ (Ab - An) of 0.1±0.05 indicates that only about 15% of the plagioclase data could be in equilibrium with a liquid of such composition. Within this range of permissible equilibrium pairs, no clear relation is evident between textural position (high An cores vs. rims), indicating that the crystals did not originally grow from a liquid represented by the bulk rock composition. To test the hypothesis that the plagioclase rims were in equilibrium with the andesitic-dacitic carrier melt and that the cores grew from more mafic liquids, we used an analogous approach to the cpx-melt model described above. The major element composition of the melt was systematically varied from 50 to 70 wt. % SiO_2 using the three exponential models (Fig. 9) and the resulting $K_D^{plag-liq}$ (Ab - An) was tracked as an indicator of potential equilibrium pairings. All calculations were performed with either 4 or 2 wt. % H_2O in the melt, the latter resulting in temperature estimates typically 60°C higher. These model calculations show that plagioclase rims (An_{55-67}) of the 2020-21 La Soufrière ejecta are consistent with the reconstructed andesite carrier melt as an equilibrium liquid for melt water contents of 4 wt.%, while calculations with 2 wt.% H_2O would indicate melt compositions with median of 53 wt.% SiO_2 (Fig. 14a). Plagioclase cores (An>70) are consistent with crystallisation from basaltic-to-basaltic andesite melts for both 2 and 4 wt. % H_2O. Modelled equilibrium pairs for plagioclase cores at 4 and 2 wt. % H_2O yield median temperatures of 1018°C and 1040°C, respectively (Fig. 14b). Plausible plagioclase rim-carrier melt equilibration temperatures for 4 wt. % H_2O show an interquartile (IQR) range between 969 and 993°C and are cooler than for 2 wt. % H_2O, which yields an IQR of 1062-1071°C. However, calculation results at 2 wt. % H_2O are not consistent with the andesitic-dacitic

composition of the carrier melt. No systematic differences are found between crystal types or between dome and scoria samples. In summary, plagioclase rim crystallisation at 4 wt.% H_2O and temperature of 982^{+11}_{-13}°C (median±IQR) matches the andesitic to dacitic composition of the reconstructed carrier melt and maximum H_2O content determined by melt inclusion analysis, and is fully consistent with the pre-eruptive temperature obtained from clinopyroxene thermometry (997^{+18}_{-35} °C).

Olivine diffusion timescales

Timescales of the processes leading up to the 2020-21 eruption can be reconstructed leveraging the diffusive exchange of Fe-Mg in olivine crystals. To constrain the temporal evolution of Fe-Mg exchange in olivine crystals, the diffusion equation (e.g. Zhang, 2010) was solved in one dimension as:

$$\frac{\partial \Phi_{XMg}}{\partial t} = D\ \frac{\partial}{\partial x}\left(\frac{\partial \Phi_{XMg}}{\partial x}\right) (1),$$

where Φ_{XMg} is the molar ratio of Mg relative to Fe and Mg (XMg = [Mg/(Mg + Fe^{2+})]), D is the diffusion coefficient for Fe-Mg exchange in olivine (Dohmen and Chakraborty 2007), t is time in seconds, T is temperature in Kelvin, and x is distance in m. Equation 1 was discretized in MATLAB using a second order explicit finite difference method. The number of numerical grid points and timestep, which are critical for the accuracy of this technique, were chosen based on convergence tests. Diffusion coefficients were calculated as (Dohmen and Chakraborty 2007):

$$D_{FeMg} = 10^{-9.21} \times (fO_2 \times\ 10^7\ )^{\frac{1}{6}}\ 10^{3(XFa-0.1)}\ e^{-\frac{201000+(P-10^5)7\times10^{-6}}{RT}}\ (2)$$

along the crystallographic c-axis [001], where fO_2 is the oxygen fugacity, XFa is the molar fayalite content in olivine, P is pressure in Pascals, R is the gas constant, and T is temperature in Kelvin. Diffusion coefficients along the crystallographic a- [100] and b-axes [010] in olivine were obtained by multiplication of equation 2 by 1/6 (Chakraborty 2010). As the diffusion coefficients depend on the olivine composition (XFa in equations 2), D was evaluated between the numerical nodes to maintain the second order accuracy of the calculations. The initial profiles and diffusivity variation along the traverse were specified based on electron microprobe analysis and linearly interpolated as step-functions on the numerical grid. The outer boundaries in the numerical model were fixed at the initial values. This approach assumes that the crystal exchanges Fe and Mg with an infinite reservoir of melt on the left boundary (i.e. outermost crystal rim). As diffusion affects only the crystal rims, we

used a fixed initial value in the outer boundary of the crystal core. If not stated otherwise, all initial profiles were modelled as a constant initial crystal composition based on the average X_{Mg} of the observed crystal core for each profile. At the start of diffusion, the outermost numerical node was fixed at the observed rim composition and the melt composition was treated as an infinite reservoir in exchange with the crystal and assuming no crystal growth.

Diffusion timescales were calculated for four profiles on three olivine crystals (sample LS21-38) from the explosive phase of the eruption (Fig. 15). Most crystals in our sample set exhibited prominent embayment textures or had thin evolved rims, indicating that olivine composition was exchanging Fe and Mg by diffusion with the carrier melt prior to eruption. Pre-diffusion initial conditions in the crystal were modelled as flat profiles in accordance with core compositions at some distance from the rim. To fully assess the uncertainty, modelling was done at three different temperatures for each profile corresponding to the median, 5th and 95th percentile of the plagioclase rim thermometry distribution (982^{+23}_{-31} °C), which is in good agreement with the temperature range indicated by cpx thermometry. As the crystallographic orientation of grains was not constrained, Fe-Mg exchange for each analysed profile was modelled using the coefficients applicable for diffusion along the c-axis [001], as well as the a- [100] and b-axes [010] (Chakraborty 2010), thereby fully capturing the 6-fold uncertainty resulting from diffusion anisotropy. The best-fit models were calculated based on minimization of squared residuals between the observed and modelled profiles. Timescale estimates range from seven months to eight years with good correspondence between two macrocrysts and profiles on the opposite sides of the same crystal (Fig. 15a-c). An olivine crystal located at the margin of a xenolith (Fig. 15d) records timescales of only 1 to 14 days. The reconstructed timescales are maxima given that crystal growth may have contributed to observed zonation features.

Discussion

Structure of the magma feeding system

Thermobarometric reconstructions of pre-eruptive magmatic variables by means of mineral-melt equilibrium modelling allow us to make inferences about the architecture of the magmatic feeding system prior to the 2020-21 eruption of La Soufrière. Although the governing relations of glass and melt inclusion chemistry for St. Vincent permit the presence of a range of basaltic andesite to andesite liquids in the sub-volcanic system, our use of all permissible equilibrium cpx-melt pairs returns strikingly consistent thermobarometric results when compared to estimates based on reconstructed groundmass compositions. Machine-learning thermobarometry suggests that most cpx crystals last equilibrated with an andesitic-dacitic carrier melt at T= 997^{+18}_{-35} °C and P= 2-3.5 kbar.

The density-depth model of Melekhova *et al.* (2019) for St. Vincent (Fig. S3) shows that these pressures are equivalent to 8-13 km depth, which we interpret as the location of a major intrusive complex beneath the volcano. This depth range lies between the magma accumulation pressures of 4 and 1-2 kbar (Fedele *et al.;* 2021) estimated for historic eruptions beneath La Soufrière volcano by comparing xenolith and bulk-rock compositions with petrological experiments (Pichavant *et al.* 2002; Pichavant and Macdonald 2007; Melekhova *et al.* 2015, 2019). The mineral compositions retrieved from our 2020-21 sample set are similar to those representing historic activity, suggesting that no major changes in the architecture of the plumbing system have occurred at least over the last few hundred years within the resolution of the different thermobarometric reconstruction approaches.

Extreme chemical zonation in plagioclase crystals, a typical feature of both St Vincent and the Lesser Antilles in general (Melekhova *et al.* 2017; Fedele *et al.* 2021; Higgins *et al.* 2021), suggests that the feeding system is characterised by multi-level magma storage. Plagioclase crystals from the 2020-21 eruption show two distinct compositional groups, represented by crystal rims (An_{55-67}) and cores of An_{80-95}, which can be linked to shallower and deeper crystallisation levels respectively. Plagioclase-melt modelling (Fig. 14a) shows that crystal core compositions are consistent with derivation from basalt or basaltic andesite liquids at temperatures of 1020-1050°C, slightly higher than inferred from cpx thermometry. Importantly, although estimates of the water content using both the volatile by difference method and H_2O analysis of primitive melt inclusions (Bouvier *et al.* 2010) point towards 4 wt.% for La Soufrière magmas, H_2O contents during mid-crustal magma crystallisation may have been significantly higher if volatile saturation was achieved at greater depth than pre-eruptive magma storage. Specifically, high water contents in crystallising melts and resulting suppression of plagioclase crystallisation are required to explain the trend of Al_2O_3 enrichment observed for lavas from La Soufrière (Melekhova *et al.* 2015). Petrological experiments at 4 kbar on basaltic andesite compositions from Montagne Pelée (Martinique) (Pichavant *et al.;* 2002) show that An contents >85 typically require H_2O contents of >5 wt.% at temperatures of 1025°C. Similarly, the Al_2O_3-based glass hygrometer of Parman *et al.* (2011) suggests a minimum H_2O content of 5.75 wt % for a maximum Al_2O_3 content of 20 wt.%. Given that An content in plagioclase is more sensitive to pH_2O than total pressure (Frey and Lange 2011; Cashman and Blundy 2013), and considering typical values for water solubility in basaltic melts (e. g. Newman and Lowenstern 2002), both mid crustal (~4 kbar) and shallow crustal (~2 kbar) crystallisation may explain the high An cores. BSE images, however, show that plagioclase cores typically have sharp facetted boundaries rather than progressive crystallisation to lower An contents in rims, which suggests a two-stage crystallisation process. Taken together, these observations suggest growth of high An cores in basaltic andesite liquids in a mid-crustal magma accumulation

zone and formation of less calcic rims upon ascent and emplacement at 2-3 kbar. The consistently lower An contents of rims compared to crystal cores is inconsistent with growth from a more primitive melt.

Relatively high Ti contents in plagioclase rims compared to cores (Fig. 6c) point to either equilibrium crystallisation in a melt of similar composition (Bindeman *et al.* 1998; Dohmen and Blundy 2014) or rapid disequilibrium growth induced by high rates of decompression or cooling (Iezzi *et al.* 2014; Mollo and Hammer 2017). The latter effect is clearly observed in the microlite population of the 2020-21 eruption in our dataset (see also Frey et al., this volume), which shows higher FeO_t and TiO_2 and lower An contents than measured in crystal rims (Fig. 6). In either case, the strong normal plagioclase zonation likely formed in response to changes in H_2O content resulting from decompression of ascending magma rather than drastic changes in melt composition. Strong zonation textures in plagioclase contrast with the homogeneous pyroxene population, which, based on our thermobarometric estimates and textural relation with plagioclase rims, have grown only in the shallow (2-3 kbar) part of the subvolcanic plumbing system. Conversely, olivine reaction rims and coronas, as well as touching relations of plagioclase cores and pristine olivine grains in troctolite xenoliths (Fig. 4), indicate that olivine was unstable in the andesitic to dacitic melt of the upper storage region and probably originated at the depths of plagioclase core formation, in which more mafic melt compositions prevailed. This interpretation is consistent with the findings of Frey et al. (this volume), suggesting that high An plagioclase and olivine microlite assemblages in the explosive deposits correspond to a deeper magma source.

Comparison to monitoring constraints

Preceding dome growth, low-level seismic signals were detected starting in November 2020, a few weeks before the dome-forming eruption began (Joseph et al., 2022). In 2021, two swarms of volcano-tectonic earthquakes detected on 23-24th March had located depths mostly shallower than 5 km. On 5-6th April 2021, shortly before the sequence of explosive eruptions began, the earthquake locations abruptly transitioned to depths of ~10 km (Joseph et al., 2022). This seismic transition was followed by a rapid, but unquantified, acceleration in dome growth and the occurrence of banded tremor (i. e. tremor bursts separated by periods of quiescence; Cabras et al., 2012) that lasted from the 8th of April until the first explosion at 08:51 local time on the 9th of April (Stinton, et al., this volume, Joseph et al., 2022). The observed progression of earthquake depths to ~10 km observed prior to the explosive phase of the eruption agrees well with our clinopyroxene thermobarometry estimates of the topmost part of the magma source region that fed the eruption (2-3 kbar; 997^{+18}_{-35} °C). We therefore suggest that the seismic swarm preceding the explosive phase of the eruption was likely an expression of increased fracturing of the overlying rock burden and continued

opening of a new conduit prior to fast magma ascent to the surface. This is corroborated by the observed increase in heat flux in the lead-up to the explosive eruption (Thompson *et al.* 2022).

Gas emissions during the eruption were monitored from the summit and offshore traverses using UV spectrometer and MultiGAS instruments, complemented by satellite-based measurements (Joseph et al., 2022; Esse et al., this volume; Taylor et al. under review). Only minor SO_2 was detected by ground-based instruments during the effusive phase of the eruption, with gas plume compositions dominated by a hydrothermal signature (Joseph et al., 2022). On 8th of April 2021, one day before the onset of explosive activity, ground- and satellite-based instruments (TROPOMI on Sentinel-5P) detected a major change in plume chemistry, with SO_2 mass flux of 80-120 tonnes/day (Joseph et al. 2022; Esse et al., this volume). During the explosive phase (9th to 22nd April) SO_2 emissions of between 29 and 562 kilotonnes/day were detected by satellite measurements (Esse et al., this volume). Following the method of Devine *et al.* (1984), petrological estimates of the mass fluxes of SO_2 during volcanic eruptions can be calculated as:

$$m(SO_2) = M\ (S_{MI}\ S_{GM}) \frac{MW(SO_2)}{MW(S)}\ (1 - XF),$$

where M is the erupted mass, S_{MI} and S_{GM} are the S contents of melt inclusions and groundmass, MW is the molecular weight of SO_2 and S, and XF is the fraction of crystals. In the calculation we use the maximum S content of 266 ppm (relative uncertainty 47%) measured in melt inclusions, a crystal fraction of 0.45, andesitic melt densities between 2300 and 2500 kg m^{-3} and assume a retardation between 30 and 200 ppm S in the groundmass based on observations at other volcanic systems with a wide range of groundmass compositions, ranging from basaltic andesitic to rhyolite (e. g. Self and King 1996; Witter *et al.* 2004; Edmonds *et al.* 2001). For a maximum lava dome volume of 18 million m^3 (Joseph et al., 2022) extruded over a period of 103 days, this results in potential SO_2 mass fluxes between 29 and 113 tonnes/day. These calculations assume 100% degassing efficiency and no scrubbing of SO_2 by the hydrothermal system. Due to the highly pulsatory nature of SO_2 emissions during the explosive phase, gas monitoring and petrological estimates are more difficult to compare. We note, however, that the maximum magma S content of 660±290 ppm estimated by Esse et al. (this volume), derived from mass eruption rates and peak SO_2 fluxes on April 11th 2021, agrees within uncertainty with the magma S content based on melt inclusions.

Several distinct types of ground deformation were detected by GPS and interferometric synthetic-aperture radar (InSAR) both before and during the eruption and modelled to constrain source depths by Camejo-Harry et al. (this volume). Deep crustal inflation, modelled with a Mogi-source depth of 18 km, was detected in the six months before dome extrusion began and continued

after lava effusion commenced. In the first few days of explosive activity, strong subsidence was observed and modelled with a Mogi-source at 6 km depth (Camejo-Harry et al. this volume). These estimates independently corroborate the interpretation based on plagioclase zonation textures and chemistry that the magma feeding system of La Soufrière is multi-layered. The inferred subsidence source depth preceding the explosive phase is shallower compared to our depth estimate for the magma source based on cpx barometry (mean: 9.5 km depth; preferred range: 8 to 13 km) but overlaps with the deflation source within uncertainty of both methods. Although petrological analysis combined with experimental data (Pichavant *et al.* 2002) permits only an approximation of the depth estimate for the deeper magma storage region, the duality of crustal deformation signals hints towards a possible link to the strong bimodality in plagioclase zonation that is characteristic of La Soufrière St Vincent magmas. A Mogi-source depth of 18 km for pre-eruption inflation translates to ~5 kbar pressure (Melekhova et al. 2019). We suggest that this depth corresponds to the lower storage region where plagioclase cores and troctolite xenoliths originate. This comparison shows the power of combining petrological and geophysical studies, although further work is required to better resolve the geometry of the La Soufrière St Vincent magmatic feeding system.

Initiation of the 2020-21 eruption

Mafic magma recharge, remobilisation of previously intruded magma, reactivation of the system by volatile fluxing and incoming felsic melt could all be invoked to explain the renewed activity at La Soufrière. These different scenarios can be tested using our mineral chemical data. Recharge of magma bodies with (typically) more primitive melt is frequently observed at arc volcanoes and widely recognized as a process that can generate sufficient overpressure to initiate volcanic eruptions (e.g. Morgan *et al.* 2006; Ruprecht and Wörner 2007; Kent *et al.* 2010; Degruyter *et al.* 2016; Morgavi *et al.* 2017; Ubide *et al.* 2019; Weber *et al.* 2020; Caricchi *et al.* 2021). As discussed above, however, there is no evidence in crystals of a temperature increase or introduction of mafic melt that would suggest an important role of magma recharge prior to the 2020-21 eruption (Fedele *et al.* 2021).

Alternatively, leftover degassed magma from eruptions in the 1970s may have been remobilised. This hypothesis is an attractive explanation of the initial lava coulée formation, particularly as, in contrast to the explosive phase, only low levels of seismic and degassing unrest were detected prior to dome extrusion that might indicate the formation of a new conduit and syn-eruptive gas emissions were low (Joseph et al. 2022; Thompson et al. 2022; Esse et al. this volume). Similar scenarios of magmatic plug remobilisation within a shallow conduit have been proposed at other basaltic andesite volcanoes (Utami *et al.* 2022). A dynamical flow model for St. Vincent

(Stinton et al., this volume) suggests viscosities of ~10^{10} – 10^{11} Pa s for the lava dome and 10^{6} – 10^{7} Pa s for the explosive magma. The higher viscosities were interpreted as remnant degassed and partially crystallised magma still present in the shallow conduit pushed out during the effusive phase by the more gas-rich magma that caused the explosive eruption. However, our petrological data show that the plagioclase and pyroxene macrocrystal cargo of 2020-21 eruptive products from both phases of the eruption formed at similar storage conditions and do not show any textural signs of re-equilibration at shallow depth. Remobilisation of the dome-forming magma therefore requires formation of the microlite-rich groundmass of the dome magma prior to remobilisation. In such a scenario, groundmass crystals may have shielded macrocrystal rims from remnant melt pools, effectively preventing re-equilibration. Independent of the triggering mechanism, remobilisation of vestigial 1979 magma (as opposed to solidified rock) in the shallow volcanic conduit has thermal constraints.

Typical volcanic conduit diameters are on the order of 40-60 m with the largest conduits reaching 100-200 m (Kolzenburg *et al.* 2019). However, assuming a cylindrical geometry, diameters of 40-60 m would involve unreasonable conduit lengths of 14.4 and 6.4 km to satisfy the 18 million m^3 of extruded dome lava (Joseph et al. 2022). Larger conduit diameters of 80-100 m are more compatible with the volumetric constraint and the shallow crustal seismicity (<5 km depth) observed during lava effusion (Joseph et al., 2022). Sustaining a sufficiently large volume of magma (T>950°C) in the shallow crust (geothermal gradient = 50-150°C/km) over a period of 40 years since the 1979 La Soufrière eruption requires initial conduit diameters >140 m and length of 3-4 km (supplementary Fig. S3). Although dike-like geometries may result in shorter conduit length, cooling takes place mostly through the sides, which requires similar dike thicknesses to the cylindrical conduit diameters invoked above. Remobilisation of leftover magma from previous eruptions would therefore require either significant undercooling of interstitial melt below the solidus or a large (>140 m) conduit. In either case, our petrological analysis neither refutes nor supports this hypothesis but adds the conditional constraint that the dome magma must have been extruded with an interstitial melt fraction of 10 to 20% to explain the lack of textural re-equilibration of crystal rims that would be expected in protracted storage and subsequent remobilisation.

The strong volcano-tectonic earthquake swarm propagated to ~10 km depth (Joseph *et al.* 2022); pre- and syn-eruptive deformation occurred at about 18 and 6 km (Camejo-Harry *et al.* this volume). These precursory signals point towards deeper level magmatic processes as important in the initiation of the explosive eruption. From a petrological perspective, the lack of evidence for pre-eruptive re-heating or interaction of crystal cargo with a compositionally contrasting melt in the

storage region (8-13 km) indicates eruption initiation by gas- or buoyancy driven internal processes that were intrinsic to the andesitic-dacitic carrier melt. The abundance of antecrystic material in the form of glomerocrysts, and plutonic xenoliths additionally indicates the importance of magma-mush interaction. We propose that a plausible mechanism for the renewed volcanic activity is mobilisation of crystal-rich basaltic andesite magma at about 10 km depth, likely in response to destabilisation or pressurization of a deeper level andesitic melt layer (Fig. 16). Entrainment of troctolite xenoliths in the explosive phase of the eruption with unzoned high An crystals that are similar to macrocrystal plagioclase cores, as well as the greater abundance of olivine and high An microlites in the initial explosive phase (Frey *et al.* this volume), suggests that there is a deep component in this phase of the eruption that may correspond to the 18 km deformation source (Camejo-Harry *et al.* this volume). The presence of deep-derived melt and troctolite together with plag-opx-cpx-tmt mush fragments from the storage level at ~10 km depth, indicates an important role of melt-mush interaction.

The andesitic-dacitic carrier melt can originate by compaction-driven extraction of interstitial melt during crystallisation and interaction of recharging melts or volatiles (Dufek and Bachmann 2010; Parmigiani *et al.* 2014; Pistone *et al.* 2017; Hartung *et al.* 2019), percolative reactive flow through crystal mush (Solano *et al.* 2012; Jackson *et al.* 2018) or partial melting of previously intruded gabbro (Melekhova *et al.* 2015). Regardless of the formation mechanism, however, buoyant melt-rich layers can develop gravitational instabilities in crystal mushes that cause melt ascent to shallower levels or, ultimately, to the surface (Seropian *et al.* 2018; Sparks *et al.* 2019). For andesitic melt lenses in crystal mushes with viscosity of 10^{14} to 10^{15} Pa s, instability timescales of several decades to centuries can be expected (Seropian *et al.* 2018), consistent with the eruptive behaviour observed at St Vincent over historical time. In summary, intrusion of deeper-derived andesite melt accompanied by disintegration of crustal cumulates and crystal mush is consistent with the petrological characteristics of the 2020-21 eruption of La Soufrière St Vincent.

Timescales of magma-mush interaction

Diffusion modelling of olivine in the 2020-21 scoria reveals that crystals were entrained in the carrier melt both prior to and during eruption. Additionally, although our preliminary calculations are subject to large uncertainties, modelling results indicate that individual crystals spent different periods of time in the carrier melt prior to eruption. Timescales on the order of days to weeks are likely related to the breakup of olivine-bearing xenoliths entrained by the andesitic-

dacitic melt during the eruption, as previously described from St. Vincent (Arculus and Wills ,1980; Tollan *et al.* 2012; Melekhova *et al.* 2019). Calculated timescales of months to years extend the interaction timescale between carrier melt and olivine cargo to the pre-eruptive period, and before the detection of seismic unrest prior to the explosive eruption. These timescales suggest that mush-carrier melt interaction is a driver, rather than a consequence, of the eruption.

Less intense seismic flurries also occurred during the pre-eruptive episode at La Soufrière (Thompson *et al.* 2022). Indeed, plagioclase residence times modelled for the 1979 eruption suggested entrainment of crystals in the melt 100 to 450 years prior to eruption (Zellmer *et al.* 1999). While these timescales are longer than our estimates, these are maxima due to uncertainty in the initial plagioclase trace element concentrations. ^{238}U-^{230}Th isochrons from St Vincent cumulate xenoliths suggest crystal residence times on the order of tens of thousands of years (Heath et al., 1998b). Old radiometric ages and short diffusion timescales are commonly observed in magmatic systems (Cooper and Kent, 2014). Importantly, they are not mutually exclusive as in-growth of radioisotopes and diffusive re-equilibration are activated by different processes (gradients in chemical potential/temperature versus radioactive decay). For this reason, it is not uncommon for arc magmas to have crystals with old U-Th ages and young rims (Cooper and Kent 2014; Cashman *et al.* 2017). Although not their favoured explanation, Heath et al. (1998b) showed that remobilisation of old intruded crystals by a 'zero-age' melt can explain the U-Th isochron data. A more detailed study of olivine diffusion timescales in all phases of the recent eruption is required to assess whether olivine age distributions can be related to large regional earthquakes that may have contributed to the destabilisation of the magma feeding system and mobilisation of melts and cumulate piles beneath St Vincent.

Transition in eruptive style

Petrological evidence for the transition from effusive to explosive activity during the 2020-21 eruption is remarkably sparse in the analysed sample set. Our finding that macrocrysts mineral chemistry, pressure and temperature estimates are indistinguishable for the dome and scoria samples, together with the similar macrocryst contents of the erupted rocks, suggest no major difference in storage conditions prior to the final ascent during the explosive eruptions. Given these similarities, it seems unlikely that differences in magma viscosity at depth or initial volatile content caused the effusive-explosive transition at La Soufrière. However, as noted above, the observed eruption transition may record when dome magma in the shallow conduit at high crystallinity, and in

a mostly degassed state, was extruded by deeper gas-rich magma, which caused a transition in eruptive style once the deep magma reached the surface (Stinton et al. this volume; Sparks et al. this volume). However, the age of this earlier magma is not constrained by the petrological data and may have been intruded subsequent to the last eruption in 1979.

Alternatively, gas loss during slow aseismic ascent of the dome magma from the storage zone at 8-13 km, followed by rapid (gas-retaining) ascent could explain the common characteristics of microcrystal assemblages in the effusive and explosive phase. Here the contrasting intensity of seismic unrest prior to both phases of the eruption is explained by differing magma ascent rates, as evidenced by the rapid increase in lava extrusion rate prior to the onset of explosive activity (Stinton et al. this volume) and differences in the microlite populations of rocks erupted during different phases of the 2020-21 eruption (Frey et al., this volume). Limited seismicity during both the precursory and initial stages of lava extrusion is still consistent with ascent of the dome magma from a crustal reservoir, given observations of aseismic conduit formation at other arc volcanoes (Roman and Cashman 2018). This poses the question of why ascent rates of magmas with equivalent storage conditions would be different. We suggest that differences in ascent rates could be related to the architecture of the multi-layered plumbing system, as evidenced by the presence of deep-derived troctolite xenoliths with unzoned high An plagioclase in explosive products and deformation sources at ~18 and 6 km depth (Camejo-Harry et al. this volume). Pressurisation of the deep source may have mobilised the shallow dome-forming magma; subsequent rapid ascent of deeper gas-rich andesitic-dacitic melt could have produced the later explosive activity. This two-stage model is similar to remobilisation of leftover magma (from the 1970s or later) in the conduit but does not require formation of groundmass microlites prior to lava mobilisation. Using the microlite assemblage from earlier explosions in the 2021 sequence, Frey et al. (this volume) investigated late-stage variations in storage and ascent that could have led to these explosions.

Crucially, factors unrelated to the degassing behaviour of the magma are hard to reconcile with the observations. Although the erupted bulk-rock compositions of the explosive phase are slightly more mafic than the dome, much of this variation is controlled by the presence of partially disintegrated olivine-rich xenoliths in the latter and may simply represent sampling bias. Bulk-compositional control on eruptive style also seems unlikely because samples from the 1979 eruption record a similar chemical spread but effusive activity produced more mafic bulk-rock compositions. Melt compositional controls on viscosity (Di Genova *et al.* 2017) are also unlikely in crystal-rich basaltic andesite magmas. In contrast, textural differences between dome and explosive samples (Fig. S1), including reaction rims on olivine and pyroxenes, reacted microlites in groundmass, and

exsolution of Fe-Ti oxides in the lava dome samples, can be attributed to slow cooling and oxidation during dome emplacement (Saito *et al.* 2007; Scott *et al.* 2012; Morrison Evans et al., this volume). Given the similarity of macrocrystal compositions in effusive and explosive samples, it seems plausible that the transition in eruptive style is related to differences in ascent rates and outgassing efficiency (e. g. Cassidy *et al.* 2018). For example, if ascent is buoyancy-driven from a source region at ~10 km depth, then progressive thickening of this layer will increase buoyancy forces and increase ascent rates. We speculate that thickening of a buoyant layer by injection of andesitic melt in late 2020 and early 2021 may have played a 'bottom-up' role in driving the transition in eruptive style, although we cannot rule out a 'top-down' process such as a decompression wave propagating down the conduit in response to continued extrusion of degassed lava. Indeed, limited olivine diffusion timescales of <14 days bracket the seismic precursors to the explosive event; improved spatial and temporal sample density could further test and constrain these models. In summary, differences in magma ascent rates, likely reflecting the multi-layer architecture of the plumbing system, are consistent with the effusive to explosive transition of crystal-rich basaltic andesite magma of similar composition and physical properties. Future work could focus on better defining the relationship between olivine diffusion timescales and geophysical monitoring signals, as well as constraining the budget of volatiles such as the CO_2 content for St Vincent magmas.

Concluding remarks

1. The 2020-21 eruption of La Soufrière St Vincent is characterised by both slow extrusion and explosive eruption of crystal-rich basaltic andesite magma. The eruptive products are similar in bulk-rock composition and mineral chemistry to previous activity of the volcano, indicating that La Soufrière volcano is currently in a steady-state regime.

2. The eruption was fed by magma at about 1000°C from a reservoir between 8 and 13 km depth. Plagioclase zonation patterns indicate discrete transfer between deeper (i.e. about 18 km) and shallower levels (~8-13 km depth) of the magmatic system and show no evidence for chemical interaction or mixing of mafic and evolved melts. The shallow part of the intrusive complex beneath St Vincent is likely comprised of predominantly sub- or near-solidus material.

3. The crystal cargo was brought to the surface in an andesitic-dacitic carrier melt with water content of ≥4 wt. %. Disruption of the shallow mush reservoir by the incoming andesite is suggested by the common occurrence of xenoliths and glomerocrysts. Seismic activity extending to 10 km

depth may document breakup of previously intruded and mostly solidified magma batches followed by fracturing of the overlying rock burden.

4. Olivine crystals resided in the melt for months to years prior to the eruption and were entrained syn-eruptively by disintegration of xenoliths and show that intrusion of andesite melt into the shallow part of the feeding system occurred shortly prior to the eruption. The impact of andesite melt on the buoyancy of the system may have played an important role in its destabilisation.

5. Lava dome and explosively erupted samples are nearly identical in phase proportions and mineral chemistry with no petrological evidence for protracted sub-surface storage and remobilisation of dome-forming magmas. Differences in eruptive style at St Vincent likely reflect outgassing efficiency during magma ascent occurring at differing rates over the course of the eruption, possibly in response to changes in buoyancy forces in the source region at depth.

Acknowledgements

This study was supported by the UK Natural Environment Research Council (NERC) through an Urgency Grant (NE/W000725/1). G.W. further acknowledges funding through an Early Postdoc. Mobility Fellowship from the Swiss National Science Foundation (SNSF). J.B. acknowledges funding from a Royal Society Research Professorship (RP\R1\201048). We would like to thank S. Sparks for valuable suggestions and discussion. DMP acknowledges support from the NERC Centre for Observation and Modelling of Earthquakes, Volcanoes and Tectonics (COMET). The authors are grateful to R. Robertson and the UWI Seismic Centre for discussion and support in the field. We thank V. Smith and A. Matzen for help with electron microprobe analysis, M. Beverley-Smith for rapid thin section preparation, and R. Galbraith for preliminary petrography. We also thank B. Andrews (Smithsonian) for discussion.

CRediT author statement

Gregor Weber: Conceptualization, Investigation, Visualization, Formal analysis, Software, Writing- Original draft. **Jon Blundy**: Conceptualization, Investigation, Funding acquisition, Writing- Review & Editing. **Jenni Barclay**: Conceptualization, Investigation, Funding acquisition, Writing- Review & Editing, project administration. ***David Pyle****:* Funding acquisition (PI), Conceptualization, Investigation, project administration, Writing- Review & Editing. **Paul Cole**: Conceptualization, Investigation, Writing- Review & Editing, Funding acquisition. **Holli Frey:** Investigation, Writing- Review & Editing. **Matthew Manon:** Investigation, Writing- Review & Editing. **Bridie Davies:** Investigation. **Katharine Cashman:** Investigation and editing.

References

Andersen, N.L., Singer, B.S., Costa, F., Fournelle, J., Herrin, J.S. and Fabbro, G.N. 2018. Petrochronologic perspective on rhyolite volcano unrest at Laguna del Maule, Chile. *Earth and Planetary Science Letters*, **493**, 57–70, https://doi.org/10.1016/j.epsl.2018.03.043.

Andrews, B.J., Gardner, J.E. and Housh, T.B. 2008. Repeated recharge, assimilation, and hybridization in magmas erupted from El Chichón as recorded by plagioclase and amphibole phenocrysts. *Journal of Volcanology and Geothermal Research*, **175**, 415–426, https://doi.org/10.1016/j.jvolgeores.2008.02.017.

Arculus, R.J. and Wills, K.J.A. 1980. The Petrology of Plutonic Blocks and Inclusions from the Lesser Antilles Island Arc. *Journal of Petrology*, **21**, 743–799, https://doi.org/10.1093/petrology/21.4.743.

Aspinall, W.P., Sigurdsson, H. and Shepherd, J.B. 1973. Eruption of Soufrière Volcano on St. Vincent Island, 1971-1972. *Science*, **181**, 117–124, https://doi.org/10.1126/science.181.4095.117.

Bebbington, M.S. and Marzocchi, W. 2011. Stochastic models for earthquake triggering of volcanic eruptions. *Journal of Geophysical Research: Solid Earth*, **116**, https://doi.org/10.1029/2010JB008114.

Bindeman, I.N., Davis, A.M. and Drake, M.J. 1998. Ion Microprobe Study of Plagioclase-Basalt Partition Experiments at Natural Concentration Levels of Trace Elements. *Geochimica et Cosmochimica Acta*, **62**, 1175–1193, https://doi.org/10.1016/S0016-7037(98)00047-7.

Blake, S. 1984. Volatile oversaturation during the evolution of silicic magma chambers as an eruption trigger. *Journal of Geophysical Research: Solid Earth*, **89**, 8237–8244.

Bouvet de Maisonneuve, C., Costa, F., Patia, H. and Huber, C. 2015. Mafic magma replenishment, unrest and eruption in a caldera setting: insights from the 2006 eruption of Rabaul (Papua New Guinea). *Geological Society, London, Special Publications*, **422**, 17–39, https://doi.org/10.1144/SP422.2.

Bouvier, A.-S., Métrich, N. and Deloule, E. 2008. Slab-Derived Fluids in the Magma Sources of St. Vincent (Lesser Antilles Arc): Volatile and Light Element Imprints. *Journal of Petrology*, **49**, 1427–1448, https://doi.org/10.1093/petrology/egn031.

Bouvier, A.-S., Deloule, E. and Métrich, N. 2010. Fluid Inputs to Magma Sources of St. Vincent and Grenada (Lesser Antilles): New Insights from Trace Elements in Olivine-hosted Melt Inclusions. *Journal of Petrology*, **51**, 1597–1615, https://doi.org/10.1093/petrology/egq031.

Budd, D.A., Troll, V.R., et al. 2017. Magma reservoir dynamics at Toba caldera, Indonesia, recorded by oxygen isotope zoning in quartz. *Scientific Reports*, **7**, 40624, https://doi.org/10.1038/srep40624.

Camejo-Harry, M., Pascal, K., Euillades, P., Grandin, R., Hamling, I., Euillades, L., Contreras-Arratia, R., Latchman, J.L., Lynch, L., Ryan, G. and Jo, M. Monitoring volcano deformation at La Soufrière, St. Vincent during the 2020-21 eruption with insights into its magma plumbing system architecture. (this volume).

Caricchi, L., Sheldrake, T.E. and Blundy, J. 2018. Modulation of magmatic processes by CO2 flushing. *Earth and Planetary Science Letters*, **491**, 160–171, https://doi.org/10.1016/j.epsl.2018.03.042.

Caricchi, L., Townsend, M., Rivalta, E. and Namiki, A. 2021. The build-up and triggers of volcanic eruptions. *Nature Reviews Earth & Environment*, **2**, 458–476, https://doi.org/10.1038/s43017-021-00174-8.

Cashman, K. and Blundy, J. 2013. Petrological cannibalism: the chemical and textural consequences of incremental magma body growth. *Contributions to Mineralogy and Petrology*, **166**, 703–729, https://doi.org/10.1007/s00410-013-0895-0.

Cashman, K.V., Sparks, R.S.J. and Blundy, J.D. 2017. Vertically extensive and unstable magmatic systems: A unified view of igneous processes. *Science*, **355**, eaag3055, https://doi.org/10.1126/science.aag3055.

Cassidy, M., Castro, J.M., et al. 2016. Volatile dilution during magma injections and implications for volcano explosivity. *Geology*, **44**, 1027–1030, https://doi.org/10.1130/G38411.1.

Cassidy, M., Manga, M., Cashman, K. and Bachmann, O. 2018. Controls on explosive-effusive volcanic eruption styles. *Nature Communications*, **9**, 2839, https://doi.org/10.1038/s41467-018-05293-3.

Chakraborty, S. 2010. Diffusion Coefficients in Olivine, Wadsleyite and Ringwoodite. *Reviews in Mineralogy and Geochemistry*, **72**, 603–639, https://doi.org/10.2138/rmg.2010.72.13.

Cole, P.D., Robertson, R.E.A., Fedele, L. and Scarpati, C. 2019. Explosive activity of the last 1000 years at La Soufrière, St Vincent, Lesser Antilles. *Journal of Volcanology and Geothermal Research*, **371**, 86–100, https://doi.org/10.1016/j.jvolgeores.2019.01.002.

Cole, P.D., Barclay, J., Robertson, R.E.A., Mitchell, S., Davies, B.V., Constantinescu, R., Sparks, R.S.J., Aspinall, W., Stinton, A. Explosive sequence of La Soufrière St Vincent April 2021: insights into drivers and consequences via eruptive products. (this volume).

Cooper, G.F., Macpherson, C.G., et al. 2020. Variable water input controls evolution of the Lesser Antilles volcanic arc. *Nature*, **582**, 525–529, https://doi.org/10.1038/s41586-020-2407-5.

Cooper, K.M. and Kent, A.J.R. 2014. Rapid remobilization of magmatic crystals kept in cold storage. *Nature*, **506**, 480–483, https://doi.org/10.1038/nature12991.

Degruyter, W., Huber, C., Bachmann, O., Cooper, K.M. and Kent, A.J.R. 2016. Magma reservoir response to transient recharge events: The case of Santorini volcano (Greece). *Geology*, **44**, 23–26, https://doi.org/10.1130/G37333.1.

Devine, J.D., Sigurdsson, H., Davis, A.N. and Self, S. 1984. Estimates of sulfur and chlorine yield to the atmosphere from volcanic eruptions and potential climatic effects. *Journal of Geophysical Research: Solid Earth*, **89**, 6309–6325, https://doi.org/10.1029/JB089iB07p06309.

Di Genova, D., Kolzenburg, S., Wiesmaier, S., Dallanave, E., Neuville, D.R., Hess, K.U. and Dingwell, D.B. 2017. A compositional tipping point governing the mobilization and eruption style of rhyolitic magma. *Nature*, **552**, 235–238, https://doi.org/10.1038/nature24488.

Dohmen, R. and Blundy, J. 2014. A predictive thermodynamic model for element partitioning between plagioclase and melt as a function of pressure, temperature and composition. *American Journal of Science*, **314**, 1319–1372, https://doi.org/10.2475/09.2014.04.

Dohmen, R. and Chakraborty, S. 2007. Fe–Mg diffusion in olivine II: point defect chemistry, change of diffusion mechanisms and a model for calculation of diffusion coefficients in natural olivine. *Physics and Chemistry of Minerals*, **34**, 409–430, https://doi.org/10.1007/s00269-007-0158-6.

Druitt, T.H., Costa, F., Deloule, E., Dungan, M. and Scaillet, B. 2012. Decadal to monthly timescales of magma transfer and reservoir growth at a caldera volcano. *Nature*, **482**, 77–80, https://doi.org/10.1038/nature10706.

Dufek, J. and Bachmann, O. 2010. Quantum magmatism: Magmatic compositional gaps generated by melt-crystal dynamics. *Geology*, **38**, 687–690, https://doi.org/10.1130/G30831.1.

Edmonds, M., Pyle, D., & Oppenheimer, C. (2001). A model for degassing at the Soufriere Hills Volcano, Montserrat, West Indies, based on geochemical data. Earth and Planetary Science Letters, 186(2), 159-173.

Esse, B., Burton, M., Hayer, C., Contreras-Arratia, R., Christopher, T., Joseph, E. P., Varnam, M., and Johnson, C., SO2 emissions during the 2021 eruption of La Soufrière St. Vincent, revealed with back-trajectory analysis of TROPOMI imagery. (this volume)

Fedele, L., Cole, P.D., Scarpati, C. and Robertson, R.E.A. 2021. Petrological insights on the last 1000 years of explosive activity at La Soufrière volcano, St. Vincent (Lesser Antilles). *Lithos*, **392–393**, 106150, https://doi.org/10.1016/j.lithos.2021.106150.

Fiske, R.S. and Sigurdsson, H. 1982. Soufriere Volcano, St. Vincent: Observations of Its 1979 Eruption from the Ground, Aircraft, and Satellites. *Science*, **216**, 1105–1106, https://doi.org/10.1126/science.216.4550.1105.

Frey, H.M. and Lange, R.A. 2011. Phenocryst complexity in andesites and dacites from the Tequila volcanic field, Mexico: resolving the effects of degassing vs. magma mixing. *Contributions to Mineralogy and Petrology*, **162**, 415–445, https://doi.org/10.1007/s00410-010-0604-1.

Frey, H.M., Manon, M.R., Barclay, J., Davies, B.V., Walters, S.A., Cole, P.D., Christopher, T.E., and Joseph, E.P., Petrology of the explosive deposits from 1 the April 2021 eruption of La Soufrière volcano, St Vincent: a time-series analysis of microlites. (this volume).

Ginibre, C. and Wörner, G. 2007. Variable parent magmas and recharge regimes of the Parinacota magma system (N. Chile) revealed by Fe, Mg and Sr zoning in plagioclase. *Lithos*, **98**, 118–140, https://doi.org/10.1016/j.lithos.2007.03.004.

Graham, A.M. and Thirlwall, M.F. n.d. Petrology of the 1979 eruption of Soufriere volcano, St. Vincent, Lesser Antilles. 7.

Gualda, G.A.R., Ghiorso, M.S., Lemons, R.V. and Carley, T.L. 2012. Rhyolite-MELTS: a Modified Calibration of MELTS Optimized for Silica-rich, Fluid-bearing Magmatic Systems. *Journal of Petrology*, **53**, 875–890, https://doi.org/10.1093/petrology/egr080.

Hartung, E., Weber, G. and Caricchi, L. 2019. The role of H2O on the extraction of melt from crystallising magmas. *Earth and Planetary Science Letters*, **508**, 85–96, https://doi.org/10.1016/j.epsl.2018.12.010.

Heath, E., Turner, S.P., Macdonald, R., Hawkesworth, C.J. and van Calsteren, P. 1998a. Long magma residence times at an island arc volcano (Soufriere, St. Vincent) in the Lesser Antilles: evidence from 238U–230Th isochron dating. *Earth and Planetary Science Letters*, 15.

Heath, E., Macdonald, R., Belkin, H., Hawkesworth, C. and Sigurdsson, H. 1998b. Magmagenesis at Soufriere Volcano, St Vincent, Lesser Antilles Arc. **39**, 44.

Higgins, O., Sheldrake, T. and Caricchi, L. 2021. Quantitative chemical mapping of plagioclase as a tool for the interpretation of volcanic stratigraphy: an example from Saint Kitts, Lesser Antilles. *Bulletin of Volcanology*, **83**, 51, https://doi.org/10.1007/s00445-021-01476-x.

Humphreys, M.C.S., Blundy, J.D. and Sparks, R.S.J. 2006. Magma Evolution and Open-System Processes at Shiveluch Volcano: Insights from Phenocryst Zoning. *Journal of Petrology*, **47**, 2303–2334, https://doi.org/10.1093/petrology/egl045.

Iezzi, G., Mollo, S., Shahini, E., Cavallo, A. and Scarlato, P. 2014. The cooling kinetics of plagioclase feldspar as revealed by electron-microprobe mapping†. *American Mineralogist*, **99**, 898–907, https://doi.org/10.2138/am.2014.4626.

Jackson, M.D., Blundy, J. and Sparks, R.S.J. 2018. Chemical differentiation, cold storage and remobilization of magma in the Earth's crust. *Nature*, **564**, 405–409, https://doi.org/10.1038/s41586-018-0746-2.

Kent, A.J.R., Blundy, J., et al. 2007. Vapor transfer prior to the October 2004 eruption of Mount St. Helens, Washington. *Geology*, **35**, 231, https://doi.org/10.1130/G22809A.1.

Kent, A.J.R., Darr, C., Koleszar, A.M., Salisbury, M.J. and Cooper, K.M. 2010. Preferential eruption of andesitic magmas through recharge filtering. *Nature Geoscience*, **3**, 631–636, https://doi.org/10.1038/ngeo924.

Kilgour, G., Blundy, J., Cashman, K. and Mader, H.M. 2013. Small volume andesite magmas and melt–mush interactions at Ruapehu, New Zealand: evidence from melt inclusions. *Contributions to Mineralogy and Petrology*, **166**, 371–392, https://doi.org/10.1007/s00410-013-0880-7.

Kolzenburg, S., Ryan, A.G. and Russell, J.K. 2019. Permeability evolution during non-isothermal compaction in volcanic conduits and tuffisite veins: Implications for pressure monitoring of volcanic edifices. *Earth and Planetary Science Letters*, **527**, 115783, https://doi.org/10.1016/j.epsl.2019.115783.

Macdonald, R., Hawkesworth, C.J. and Heath, E. 2000. The Lesser Antilles volcanic chain: a study in arc magmatism. *Earth-Science Reviews*, **49**, 1–76, https://doi.org/10.1016/S0012-8252(99)00069-0.

McDade, P., Blundy, J.D. and Wood, B.J. 2003. Trace element partitioning between mantle wedge peridotite and hydrous MgO-rich melt. *American Mineralogist*, **88**, 1825–1831, https://doi.org/10.2138/am-2003-11-1225.

Melekhova, E., Blundy, J., Robertson, R. and Humphreys, M.C.S. 2015. Experimental Evidence for Polybaric Differentiation of Primitive Arc Basalt beneath St. Vincent, Lesser Antilles. *Journal of Petrology*, **56**, 161–192, https://doi.org/10.1093/petrology/egu074.

Melekhova, E., Blundy, J., Martin, R., Arculus, R. and Pichavant, M. 2017. Petrological and experimental evidence for differentiation of water-rich magmas beneath St. Kitts, Lesser Antilles. *Contributions to Mineralogy and Petrology*, **172**, 98, https://doi.org/10.1007/s00410-017-1416-3.

Melekhova, E., Schlaphorst, D., Blundy, J., Kendall, J.-M., Connolly, C., McCarthy, A. and Arculus, R. 2019. Lateral variation in crustal structure along the Lesser Antilles arc from petrology of crustal xenoliths and seismic receiver functions. *Earth and Planetary Science Letters*, **516**, 12–24, https://doi.org/10.1016/j.epsl.2019.03.030.

Mollo, S. and Hammer, J.E. 2017. Dynamic crystallization in magmas. *In*: Heinrich, W. and Abart, R. (eds) *Mineral Reaction Kinetics: Microstructures, Textures, Chemical and Isotopic Signatures*. 378–418., https://doi.org/10.1180/EMU-notes.16.12.

Morgan, D.J., Blake, S., Rogers, N.W., Vivo, B.D., Rolandi, G. and Davidson, J.P. 2006. Magma chamber recharge at Vesuvius in the century prior to the eruption of A.D. 79. *Geology*, **34**, 845–848, https://doi.org/10.1130/G22604.1.

Morgavi, D., Arienzo, I., Montagna, C., Perugini, D. and Dingwell, D.B. 2017. Magma mixing: History and dynamics of an eruption trigger. *Volcanic Unrest*, 123.

Neave, D.A. and Putirka, K.D. 2017. A new clinopyroxene-liquid barometer, and implications for magma storage pressures under Icelandic rift zones. *American Mineralogist*, **102**, 777–794, https://doi.org/10.2138/am-2017-5968.

Newman, S. and Lowenstern, J.B. 2002. VolatileCalc: a silicate melt–H2O–CO2 solution model written in Visual Basic for excel. *Computers & Geosciences*, **28**, 597–604, https://doi.org/10.1016/S0098-3004(01)00081-4.

Nishimura, T. 2017. Triggering of volcanic eruptions by large earthquakes. *Geophysical Research Letters*, **44**, 7750–7756, https://doi.org/10.1002/2017GL074579.

Parman, S.W., Grove, T.L., Kelley, K.A. and Plank, T. 2011. Along-Arc Variations in the Pre-Eruptive H2O Contents of Mariana Arc Magmas Inferred from Fractionation Paths. *Journal of Petrology*, **52**, 257–278, https://doi.org/10.1093/petrology/egq079.

Parmigiani, A., Huber, C. and Bachmann, O. 2014. Mush microphysics and the reactivation of crystal-rich magma reservoirs. *Journal of Geophysical Research: Solid Earth*, **119**, 6308–6322, https://doi.org/10.1002/2014JB011124.

Petrelli, M., Caricchi, L. and Perugini, D. 2020. Machine Learning Thermo-Barometry: Application to Clinopyroxene-Bearing Magmas. *Journal of Geophysical Research: Solid Earth*, **125**, e2020JB020130, https://doi.org/10.1029/2020JB020130.

Pichavant, M. and Macdonald, R. 2007. Crystallization of primitive basaltic magmas at crustal pressures and genesis of the calc-alkaline igneous suite: experimental evidence from St Vincent, Lesser Antilles arc. *Contributions to Mineralogy and Petrology*, **154**, 535–558, https://doi.org/10.1007/s00410-007-0208-6.

Pichavant, M., Mysen, B.O. and Macdonald, R. 2002. Source and H2O content of high-MgO magmas in island arc settings: an experimental study of a primitive calc-alkaline basalt from St. Vincent, lesser antilles arc. *Geochimica et Cosmochimica Acta*, **66**, 2193–2209, https://doi.org/10.1016/S0016-7037(01)00891-2.

Pistone, M., Blundy, J. and Brooker, R.A. 2017. Water transfer during magma mixing events: Insights into crystal mush rejuvenation and melt extraction processes. *American Mineralogist*, **102**, 766–776, https://doi.org/10.2138/am-2017-5793.

Putirka, K., Johnson, M., Kinzler, R., Longhi, J., & Walker, D. (1996). Thermobarometry of mafic igneous rocks based on clinopyroxene-liquid equilibria, 0–30 kbar. Contributions to Mineralogy and Petrology, 123, 92-108.

Putirka, K. (1999). Clinopyroxene+ liquid equilibria to 100 kbar and 2450 K. Contributions to Mineralogy and Petrology, 135, 151-163.

Putirka, K.D. 2005. Igneous thermometers and barometers based on plagioclase + liquid equilibria: Tests of some existing models and new calibrations. *American Mineralogist*, **90**, 336–346, https://doi.org/10.2138/am.2005.1449.

Putirka, K.D. 2008. Thermometers and Barometers for Volcanic Systems. *Reviews in Mineralogy and Geochemistry*, **69**, 61–120, https://doi.org/10.2138/rmg.2008.69.3.

Pyle, D.M., Barclay, J. and Armijos, M.T. 2018. The 1902–3 eruptions of the Soufrière, St Vincent: Impacts, relief and response. *Journal of Volcanology and Geothermal Research*, **356**, 183–199, https://doi.org/10.1016/j.jvolgeores.2018.03.005.

Robertson, R.E.A. 1995. An assessment of the risk from future eruptions of the Soufriere volcano of St. Vincent, West Indies. *Natural Hazards*, **11**, 163–191, https://doi.org/10.1007/BF00634531.

Roduit, N. (2007). JMicroVision: un logiciel d'analyse d'images pétrographiques polyvalent (Doctoral dissertation, University of Geneva).

Roman, D.C. and Cashman, K.V. 2018. Top–Down Precursory Volcanic Seismicity: Implications for 'Stealth' Magma Ascent and Long-Term Eruption Forecasting. *Frontiers in Earth Science*, **6**.

Roman, D.C., Cashman, K.V., Gardner, C.A., Wallace, P.J. and Donovan, J.J. 2006. Storage and interaction of compositionally heterogeneous magmas from the 1986 eruption of Augustine Volcano, Alaska. *Bulletin of Volcanology*, **68**, 240–254, https://doi.org/10.1007/s00445-005-0003-z.

Ruprecht, P. and Wörner, G. 2007. Variable regimes in magma systems documented in plagioclase zoning patterns: El Misti stratovolcano and Andahua monogenetic cones. *Journal of Volcanology and Geothermal Research*, **165**, 142–162, https://doi.org/10.1016/j.jvolgeores.2007.06.002.

Saito, T., Ishikawa, N. and Kamata, H. 2007. Magnetic petrology of the 1991–1995 dacite lava of Unzen volcano, Japan: Degree of oxidation and implications for the growth of lava domes. *Journal of Volcanology and Geothermal Research*, **164**, 268–283, https://doi.org/10.1016/j.jvolgeores.2007.05.015.

Scott, J.A.J., Mather, T.A., Pyle, D.M., Rose, W.I. and Chigna, G. 2012. The magmatic plumbing system beneath Santiaguito Volcano, Guatemala. *Journal of Volcanology and Geothermal Research*, **237–238**, 54–68, https://doi.org/10.1016/j.jvolgeores.2012.05.014.

Scruggs, M.A. and Putirka, K.D. 2018. Eruption triggering by partial crystallization of mafic enclaves at Chaos Crags, Lassen Volcanic Center, California. *American Mineralogist*, **103**, 1575–1590, https://doi.org/10.2138/am-2018-6058.

Self, S. and King, A.J. 1996. Petrology and sulfur and chlorine emissions of the 1963 eruption of Gunung Agung, Bali, Indonesia. *Bulletin of Volcanology*, **58**, 263–285, https://doi.org/10.1007/s004450050139.

Seropian, G., Rust, A.C. and Sparks, R.S.J. 2018. The Gravitational Stability of Lenses in Magma Mushes: Confined Rayleigh-Taylor Instabilities. *Journal of Geophysical Research: Solid Earth*, **123**, 3593–3607, https://doi.org/10.1029/2018JB015523.

Seropian, G., Kennedy, B.M., Walter, T.R., Ichihara, M. and Jolly, A.D. 2021. A review framework of how earthquakes trigger volcanic eruptions. *Nature Communications*, **12**, 1004, https://doi.org/10.1038/s41467-021-21166-8.

Shepherd, J.B., Aspinall, W.P., Rowley, K.C., Pereira, J., Sigurdsson, H., Fiske, R.S. and Tomblin, J.F. 1979. The eruption of Soufrière volcano, St Vincent April–June 1979. *Nature*, **282**, 24–28.

Solano, J.M.S., Jackson, M.D., Sparks, R.S.J., Blundy, J.D. and Annen, C. 2012. Melt Segregation in Deep Crustal Hot Zones: a Mechanism for Chemical Differentiation, Crustal Assimilation and the Formation of Evolved Magmas. *Journal of Petrology*, **53**, 1999–2026, https://doi.org/10.1093/petrology/egs041.

Sparks, R.S.J., Annen, C., Blundy, J.D., Cashman, K.V., Rust, A.C. and Jackson, M.D. 2019. Formation and dynamics of magma reservoirs. *Philosophical Transactions of the Royal Society A: Mathematical, Physical and Engineering Sciences*, **377**, 20180019, https://doi.org/10.1098/rsta.2018.0019.

Sparks, R.S.J., Aspinall, W.P., Barclay, J., Renfrew, I.A., Contreras-Arratia, R., and Stewart, R. Analysis of magma flux and eruption intensity during the 2021 1 explosive activity at the Soufrière of St Vincent, West Indies. (this volume).

Stinton, A., Sparks R.S.J., and Huppert, H.E. Analysis of magma rheology from lava spreading and explosive activity during the 2020-2021 eruption of the Soufrière St Vincent with implications for eruption dynamics. (this volume)

Stock, M.J., Humphreys, M.C.S., Smith, V.C., Isaia, R. and Pyle, D.M. 2016. Late-stage volatile saturation as a potential trigger for explosive volcanic eruptions. *Nature Geoscience*, **9**, 249–254, https://doi.org/10.1038/ngeo2639.

Taylor, I. A., Grainger, R. G., Prata, A. T., Proud, S. R., Mather, T. A., and Pyle, D. M. Satellite measurements of plumes from the 2021 eruption of La Soufriere, St Vincent. https://doi.org/10.5194/acp-2022-772 (preprint).

Tepley, F.J., Davidson, J.P., Tilling, R.I. and Arth, J.G. 2000. Magma Mixing, Recharge and Eruption Histories Recorded in Plagioclase Phenocrysts from El Chichón Volcano, Mexico. *Journal of Petrology*, **41**, 1397–1411, https://doi.org/10.1093/petrology/41.9.1397.

Thompson, J.O., Contreras-Arratia, R., Befus, K.S. and Ramsey, M.S. 2022. Thermal and seismic precursors to the explosive eruption at La Soufrière Volcano, St. Vincent in April 2021. *Earth and Planetary Science Letters*, **592**, 117621, https://doi.org/10.1016/j.epsl.2022.117621.

Tollan, P.M.E., Bindeman, I. and Blundy, J.D. 2012. Cumulate xenoliths from St. Vincent, Lesser Antilles Island Arc: a window into upper crustal differentiation of mantle-derived basalts.

Contributions to Mineralogy and Petrology, **163**, 189–208, https://doi.org/10.1007/s00410-011-0665-9.

Ubide, T., Mollo, S., Zhao, J., Nazzari, M. and Scarlato, P. 2019. Sector-zoned clinopyroxene as a recorder of magma history, eruption triggers, and ascent rates. *Geochimica et Cosmochimica Acta*, **251**, 265–283, https://doi.org/10.1016/j.gca.2019.02.021.

Utami, S.B., Andùjar, J., Costa, F., Scaillet, B., Humaida, H. and Carn, S. 2022. Pre-eruptive excess volatiles and their relationship to effusive and explosive eruption styles in semi-plugged volcanoes. *Frontiers in Earth Science*, **10**, 882097, https://doi.org/10.3389/feart.2022.882097.

Wager, L.R. 1962. Igneous cumulates from the 1902 eruption of Soufrière, St. Vincent. *Bulletin Volcanologique*, **24**, 93, https://doi.org/10.1007/BF02599333.

Walter, T.R. and Amelung, F. 2007. Volcanic eruptions following M ≥ 9 megathrust earthquakes: Implications for the Sumatra-Andaman volcanoes. *Geology*, **35**, 539–542, https://doi.org/10.1130/G23429A.1.

Wanke, M., Karakas, O. and Bachmann, O. 2019. The genesis of arc dacites: the case of Mount St. Helens, WA. *Contributions to Mineralogy and Petrology*, **174**, 7, https://doi.org/10.1007/s00410-018-1542-6.

Watt, S.F.L. 2019. The evolution of volcanic systems following sector collapse. *Journal of Volcanology and Geothermal Research*, **384**, 280–303, https://doi.org/10.1016/j.jvolgeores.2019.05.012.

Weber, G., Caricchi, L. and Arce, J.L. 2020. The Long-Term Life-Cycle of Nevado de Toluca Volcano (Mexico): Insights Into the Origin of Petrologic Modes. *Frontiers in Earth Science*, **8**, 563303, https://doi.org/10.3389/feart.2020.563303.

Witter, J.B., Kress, V.C., Delmelle, P. and Stix, J. 2004. Volatile degassing, petrology, and magma dynamics of the Villarrica Lava Lake, Southern Chile. *Journal of Volcanology and Geothermal Research*, **134**, 303–337, https://doi.org/10.1016/j.jvolgeores.2004.03.002.

Zellmer, G.F., Blake, S., Vance, D., Hawkesworth, C. and Turner, S. 1999. Plagioclase residence times at two island arc volcanoes (Kameni Islands, Santorini, and Soufriere, St. Vincent) determined by Sr diffusion systematics. *Contributions to Mineralogy and Petrology*, **136**, 345–357, https://doi.org/10.1007/s004100050543.

Zhang, Y. (2010). Diffusion in minerals and melts: theoretical background. *Reviews in mineralogy and geochemistry*, *72*(1), 5-59.

Figure Captions

Fig. 1. Context of the 2020-21 eruption of La Soufrière St Vincent. a) Location of St Vincent and other active volcanic centres in the Eastern Caribbean Arc. b) Relief map of the Island of St Vincent with major volcano-tectonic structures indicated by dashed lines. The 2020-21 lava dome in its final extent prior to destruction is indicated in orange. c) Photograph of the La Soufrière crater, containing the 2020-21 and 1979 lava domes prior to the explosive phase of the 2021 eruption. d) Eruptive plume of the 2021 explosive phase on April 9, 2021. Photographs courtesy of UWI Seismic Research Centre.

Fig. 2. Summary of textural observations of the 2020-21 eruption of La Soufrière St Vincent. a) Photomicrograph of the 2021 lava dome in plane polarized light. b) Textural features of a pyroclastic scoria clast from the explosive phase. c) High magnification back-scatter electron (BSE) image of the lava dome groundmass. Note oxidised nature of pyroxene microlites and strongly zoned plagioclase microphenocrysts (typically >20 µm) and unzoned microlites (<30 µm). d) BSE image of scoria groundmass textures. Note greater proportion of vesicles and fresher pyroxene microlites compared to (c). e) and f) BSE images of major mineral phases in lava dome samples. g) Photomicrograph (BSE) of the 2021 scoria from the explosive phase. (e) and (f) show the abrupt zoning in plagioclase phenocrysts between core and rim. Major phases and textural features are annotated as: plag: plagioclase, pyx: pyroxene, cpx: clinopyroxene, opx: orthopyroxene, ox: Fe-Ti oxide, ol: olivine, gm: groundmass, ves: vesicle.

Fig. 3. Volume percentages of different phases in the 2020-21 lava dome (orange bars) and 2020-21 scoria (green bars) samples based on random grid point-counting. Error bars on each column represent the variation (1 standard deviation) based on five thin sections. All modal percentages are presented on a vesicle free basis. Groundmass and mineral volume percent for the 1979 scoria are shown for comparison (pale pink) and have been determined based on point counting of 10 thin sections. gm: groundmass, plag: plagioclase, cpx: clinopyroxene, opx: orthopyroxene, ox: Fe-Ti oxides, ol: olivine.

Fig. 4. Back-scatter electron images of textural features of enclaves in the 2020-21 St Vincent eruption. ol: olivine, pl: plagioclase, cpx: clinopyroxene, opx: orthopyroxene, tmt: titanomagnetite. a) Troctolite enclave from the explosive phase of the eruption containing olivine and unzoned high An plagioclase. b) Large glomerocrysts with assemblage of pl-cpx-opx-tmt±ol from the lava dome. c-d) Enclaves of pl-cpx-opx-tmt±ol assemblage from the explosive phase of the eruption. Rims of strongly zoned enclave plagioclase are in contact with pyroxene crystals. Titanomagnetite occurs as eu- to subhedral crystal but also in poikilitic texture. Olivine crystals are present as remnant cores with orthopyroxene reaction coronas.

Fig. 5. Total alkali (Na_2O+K_2O) versus silica classification diagram for bulk-rock compositions of historic eruptions from La Soufrière St. Vincent. Compositional fields of basalt and basaltic andesite are marked by vertical black lines. Lava dome and scoria from the explosive phase of the 2021 eruption are shown by orange triangles and large green dots, respectively. For comparison analyses of (pre)historic activity of La Soufrière (Fedele et al. 2021), the 1902/1903 eruption (black diamonds), 1971 lava dome (blue diamonds), the 1979 effusive-explosive

eruption (pale pink squares), 1718/1812 (red diamonds), 1580 (purple diamonds), and 1440 (blue diamonds) are shown.

Fig. 6. Variation of plagioclase major element composition (anorthite content) with minor elements (FeO_{total} and TiO_2). a) Systematics of An versus FeO compared for lava dome (orange circles) and scoria (green triangles). b) Bivariate relation of An and FeO for both lava dome and scoria itemised for different crystal textures and types: Enclaves (orange squares), glomerocrysts (red diamonds), macrocrysts (rims: blue diamonds; cores: blue triangles), microlites (red crosses), microphenocrysts (purple stars). c) Inverse relationship of An and TiO_2 in lava dome plagioclase. Errors bars based on counting statistics (1sd) are shown.

Fig. 7. Relationship of enstatite content (En) and Al_2O_3 (wt. %) in 2020-21 clino- and orthopyroxenes. a) Colour coded relation for lava dome (orange circles) and explosive scoria (green triangles). b) Comparison of textural position in dome pyroxenes (rims: purple circles; cores: red circles) and scoria pyroxenes (rims: blue triangles; cores: green triangles). c) Symbols and colour coding reflecting crystal type and/or texture: Enclave hosted (orange squares), glomerocrysts (red diamonds), macrocrysts (blue circles), microlites (red crosses), microphenocrysts (purple stars). Error bars based on counting statistics are plotted in panel a). Error in En is smaller than symbol size.

Fig. 8. Forsterite (Fo) and Magnesium number (Mg#) versus distance (µm) of analysed olivine grains. Colour coding and BSE image insets show different textural groups of olivine crystals (symplectic – purple, enclave – red, macrocryst – green, remnant core - cyan). Symplectic olivine analysis are from the dome phase, while all other textural types are present only in samples from explosive phase of the eruption (U3 unit). The range of potential equilibrium olivine compositions with the carrier melt were calculated based on Blundy et al. (2020) using the most mafic reconstructed melt based on defocussed beam analysis and the most evolved melt inclusion.

Fig. 9. Bivariate plots of major element oxides (a-f) as a function of SiO_2 content. Bulk-rock analysis are shown as orange squares for the 2020-21 lava dome, and green squares for the 2021 scoria; black squares represent historic eruptions from La Soufrière (Fedele *et al.* 2021). Carrier melt composition for the 2020-21 eruption is shown as triangles for reconstructions based on mass balance approach and blue diamonds for groundmass analysis with a defocussed EPMA beam. Melt inclusions from the 2020-21 eruption are indicated by turquoise circles and grey circles for historic eruptions. The solid red line is an exponential fit through all glass inclusion data and the dashed lines represent the upper and lower prediction intervals (level=0.65) of this fit. An exponential rather than linear model was used to capture the curvature in liquid lines of descent.

Fig. 10. Assessment of clinopyroxene-melt equilibria for the 2020-21 eruption of La Soufrière. a) of the SiO_2 contents and FeO/MgO ratios in various liquids that are potentially in equilibrium with cpx: Median bulk-rock analysis (purple squares) of scoria and dome, reconstructed groundmass composition from defocussed beam analysis (pink circles, median and quartiles are shown) and mass balance (orange circle). The average melt inclusion composition is shown as

green triangle. Glass compositions of St Kitts basaltic andesite experiments (Melekhova et al., 2019) are shown for comparison. b) Mismatch between experimental and calculated temperature and pressure illustrating the validity of Kd(Fe-Mg) and Diopside-Hedenbergite error (ΔDiHd filtering criteria). Colour coding reflects if experiments are within (true: green crosses) or outside (false: black crosses) the filtering criteria based on Kd(Fe-Mg) and ΔDiHd. Pressure and temperatures were calculated using the thermobarometric model of Putirka (2008). c) Fe-Mg exchange coefficient versus distance from clinopyroxene rim for different melt compositions (bulk-rock, groundmass based on defocussed beam and mass balance, average melt inclusion). Range of equilibrium Kd(Fe-Mg) is indicated by black horizontal lines; data are coloured blue if ΔDiHd lies within the range -0.1 to 0.1.

Fig. 11. Modelling results of possible equilibrium melt - clinopyroxene pairs based on trends in melt inclusion chemistry. For a description of the modelling approach, the reader is referred to the main text section 4.4. a) Iron-magnesium exchange coefficient (Kd(Fe-Mg)) plotted versus Diopside-Hedenbergite error (ΔDiHd) for all possible combinations of cpx data and model melts. Colour coding of the model calculations reflects the SiO_2 content of the melt in weight percent. Blue rectangle shows melt-cpx pairs with permissible equilibrium conditions. b) Histogram of SiO_2 contents of the melts shown in the blue square in a.

Fig. 12. Results of clinopyroxene-liquid thermobarometry. Blue circles represent pressure (kbar) and temperature (°C) estimates based on cpx-groundmass equilibrium (defocussed beam and mass balance approach), grey triangles show cpx-melt inclusion estimates, and light blue squares are results based on the equilibrium melt modelling approach described in the main text. Pressures were converted into depth using density values applicable to the Lesser Antilles (Melekhova *et al.* 2019). Calculations were done using 4 wt.% H_2O in the melt phase. a) Estimates recovered using the cpx-liquid model of Putirka (2008) (their eqns. 30 and 33). b) Pressures and temperatures retrieved using the machine learning model of Petrelli et al., (2020).

Fig. 13. Temperature estimates based on coexisting clinopyroxene and orthopyroxene compositions. a) Temperatures (°C) and exchange coefficient (KD(Fe-Mg)) are shown for cpx-opx pairs based on equation 37 of Putirka (2008). Colour coding reflects pyroxene pairs from dome (orange diamonds) and scoria (green circles). The range of putative equilibrium KD(Fe-Mg) under magmatic conditions is shown by the grey shaded area and the range of exchange coefficients more applicable for subsolidus systems is shown in the red shaded vertical bar. b) Same data, but colour coding now reflects the type of opx-cpx pair. Blue circles represent estimates of all possible combinations of outermost rims in contact with the groundmass, touching opx-cpx grains are shown as red squares, and profiles across a touching cpx-opx boundary are shown as green diamonds.

Fig. 14. Results of plagioclase-equilibrium melt modelling and thermometry (Putirka, 2008). a) Boxplots of model melt SiO_2 content that could be in equilibrium with the observed plagioclase compositions at a melt water content of 2 wt.% (filled boxplots) and 4 wt. % H_2O (open boxplots). The number of matching plagioclase-melt pairs is indicated by n. b) Distribution of

temperatures (°C) for matching pairs of melts with plagioclase rims and cores using a water content of 4 and 2 wt. %. The modelling approach is described in the main text.

Fig. 15. Olivine diffusion modelling. Subpanels a-d show back scatter electron images with analytical traverses marked in red and corresponding Fo (mol. %) profiles on the right-hand side. The initial profile in the diffusion model is shown as solid blue line and the best-fit model as red curve. The inset in each case shows the resulting timescale estimates as a function of model temperature for diffusion along the c-axis (blue bars) and along the a or b axis (green bars). Note that while timescales in panels a-c are in months, panel c is shown in days.

Fig. 16. Conceptual summary of the proposed magma feeding system and processes leading up to the 2021 eruption of La Soufrière St Vincent. Pyroxene thermobarometry resolves a magma reservoir at 8-13 km depth that is the source of most of the crystal cargo in both phases of the eruption. Pre-eruptive deformation at depth of 18 km (Camejo-Harry et al. this volume) and the presence of troctolite enclaves containing high An plagioclase originating at greater depth suggest that pressurisation and destabilisation of a deeper magmatic reservoir was involved in the initiation of the eruption. Initial lava formation is consistent with either aseismic ascent of magma from the shallow reservoir or extrusion of leftover magma in the volcanic conduit. Intrusion of gas-rich andesite melt in the shallow reservoir containing crystals that have formed from similar melts initiated the explosive phase of the eruption.

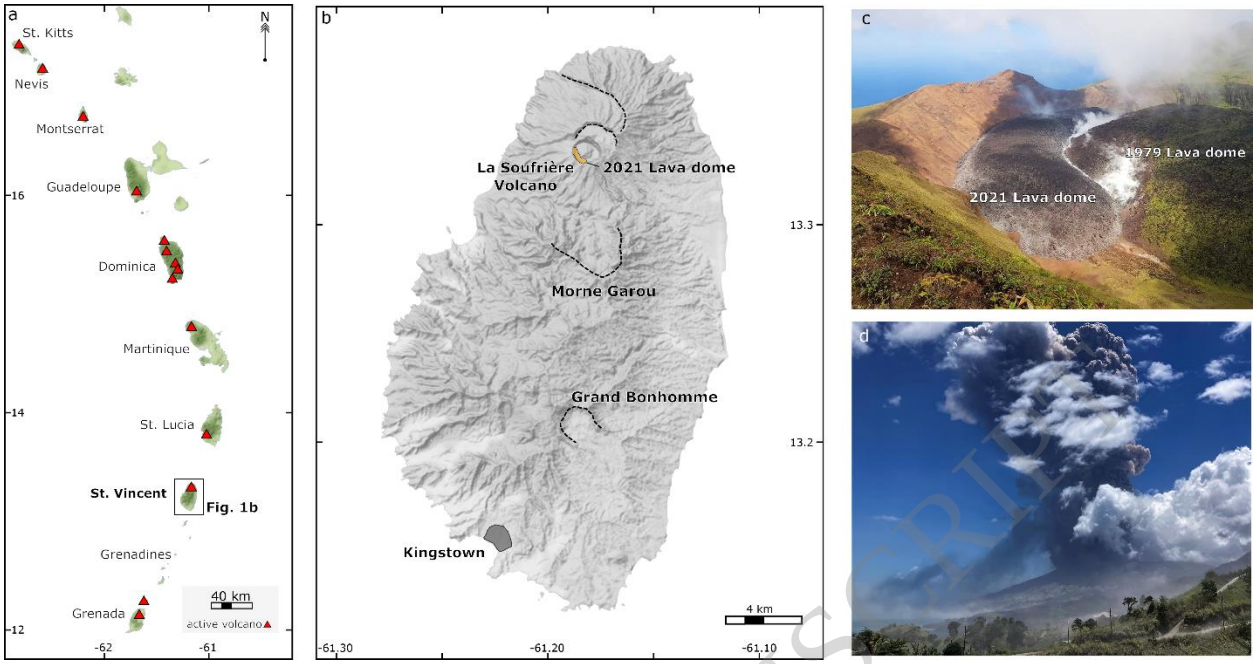

Figure 1

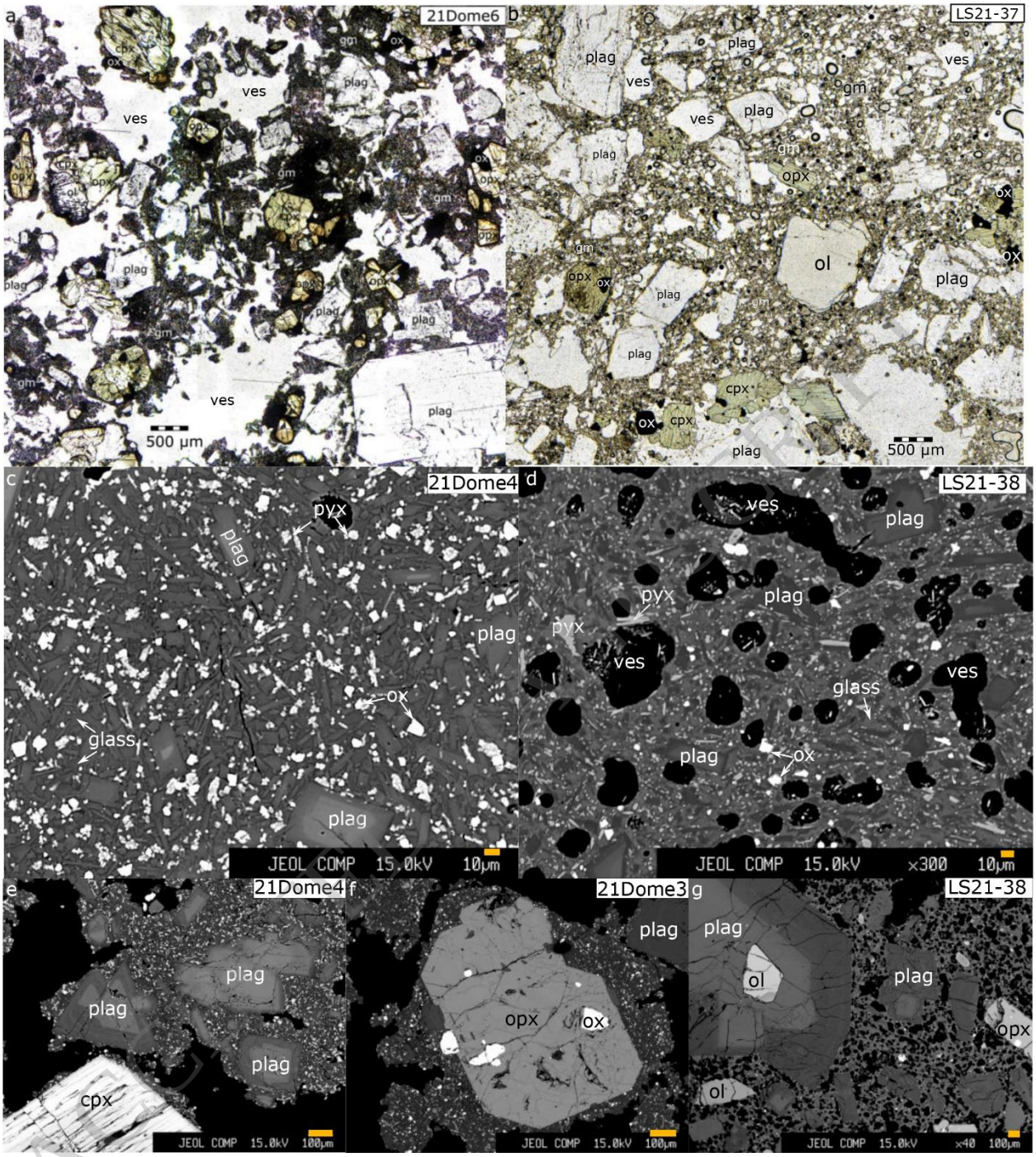

Figure 2

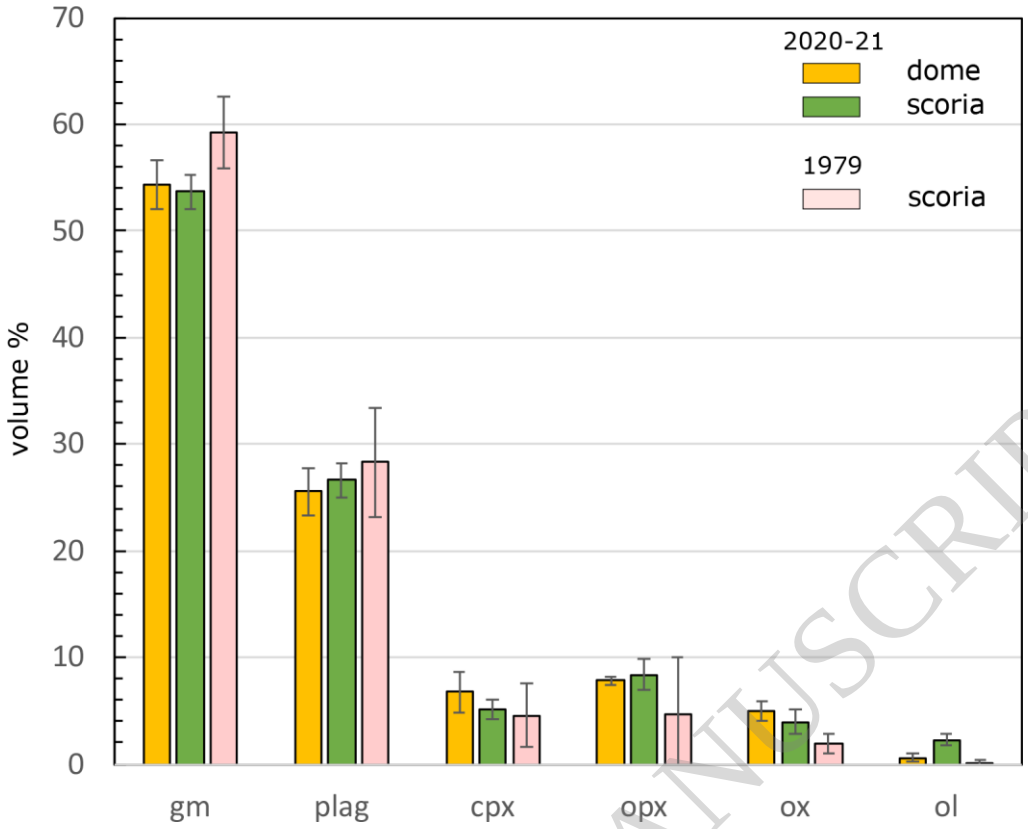

Figure 3

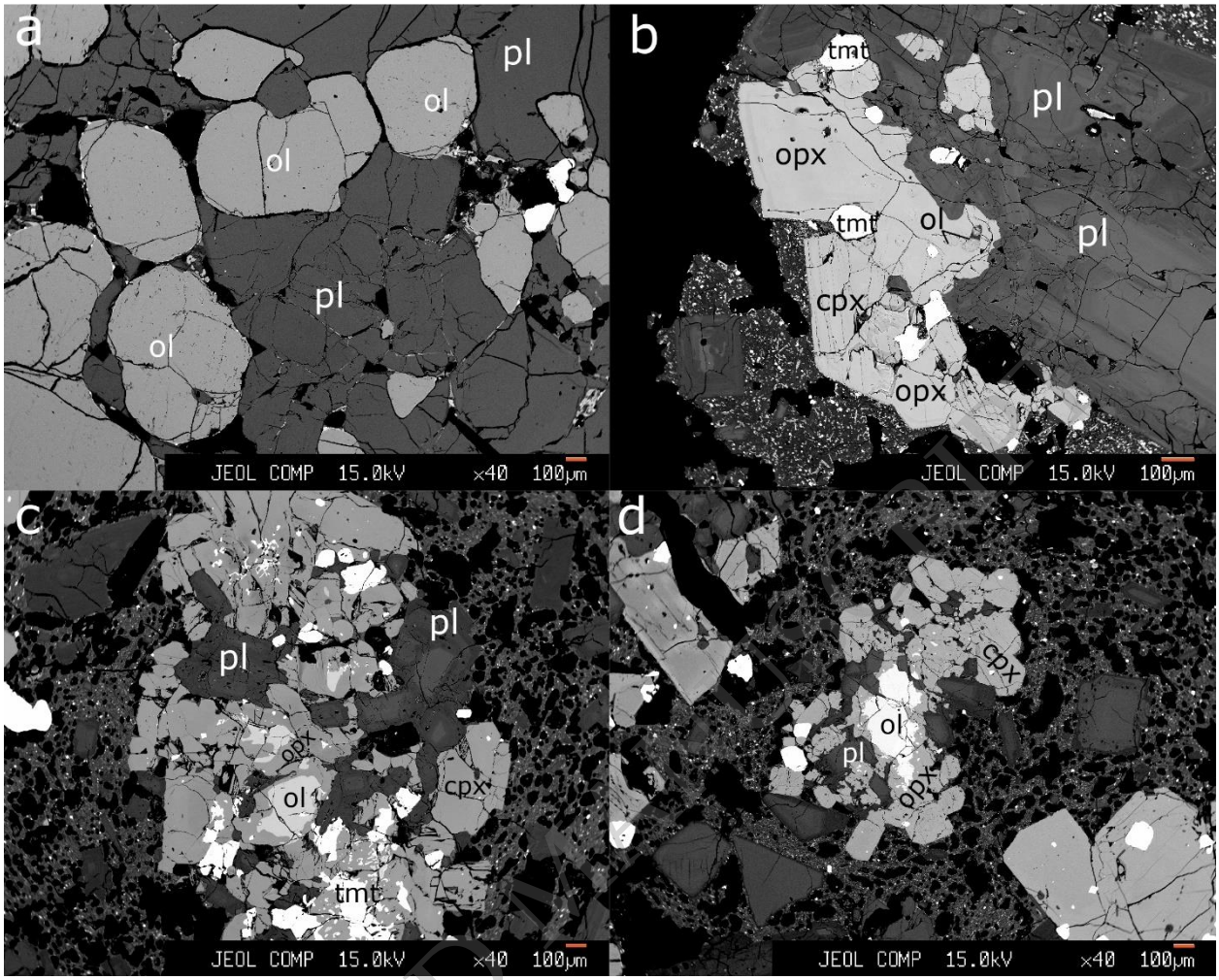

Figure 4

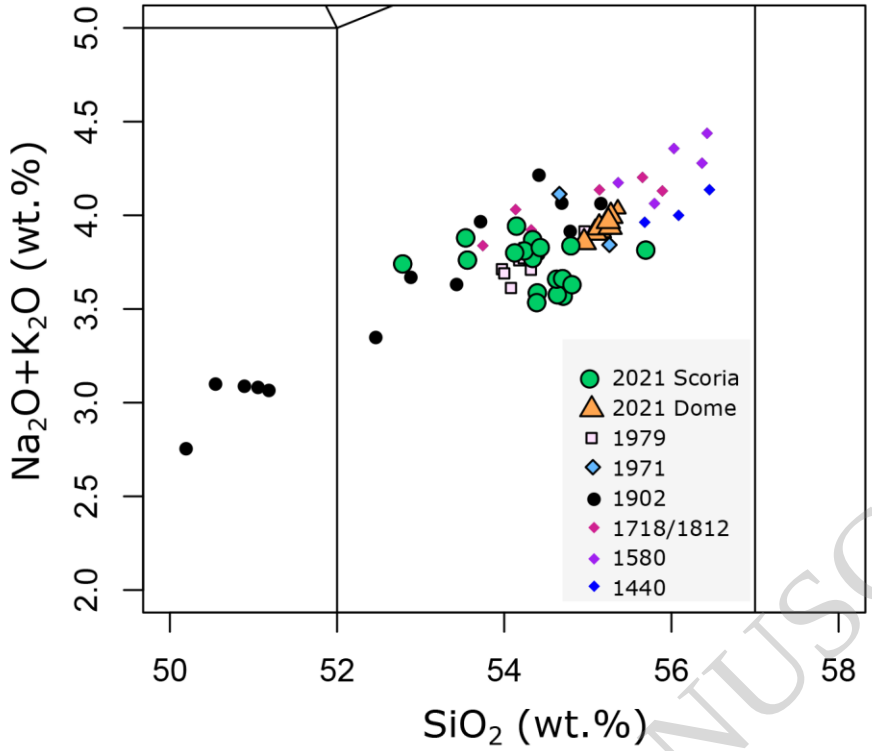

Figure 5

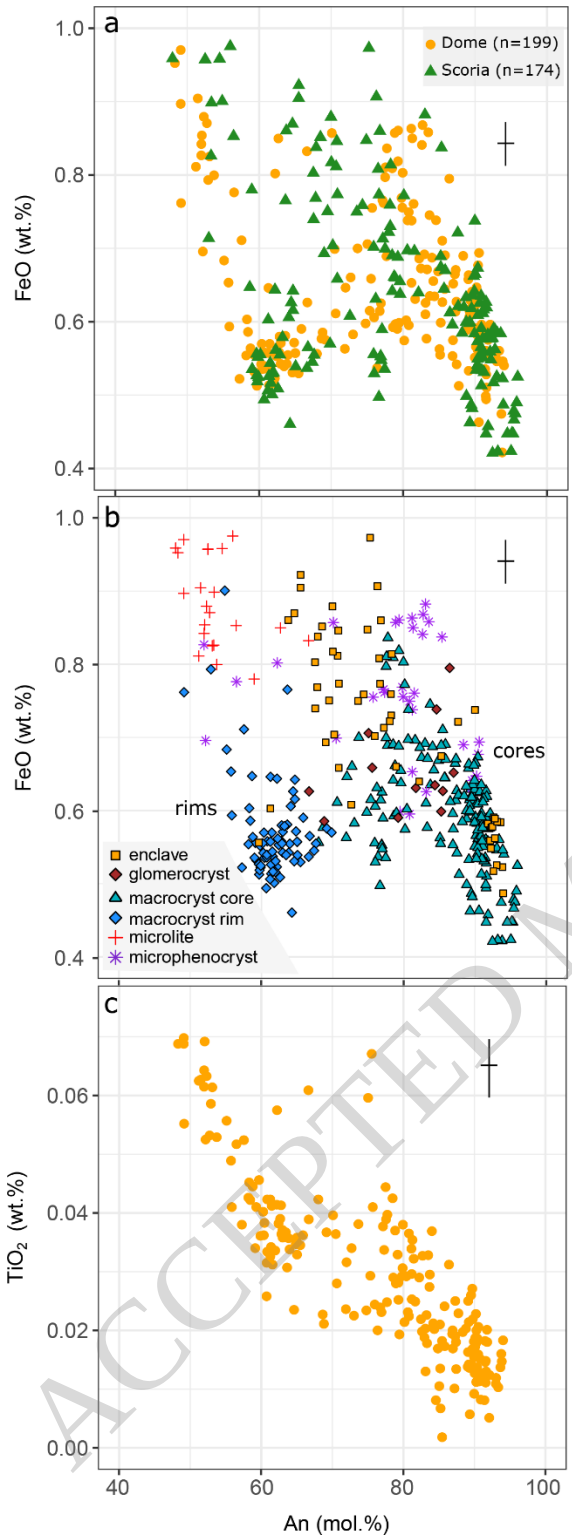

Figure 6

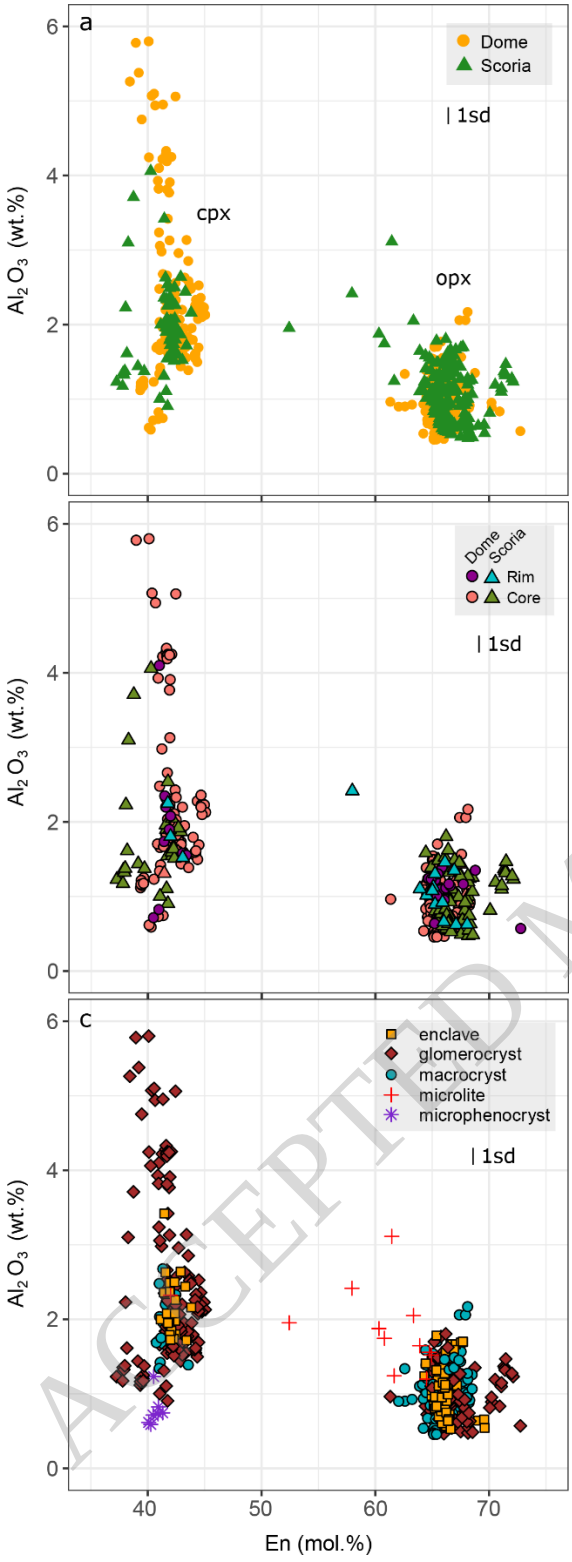

Figure 7

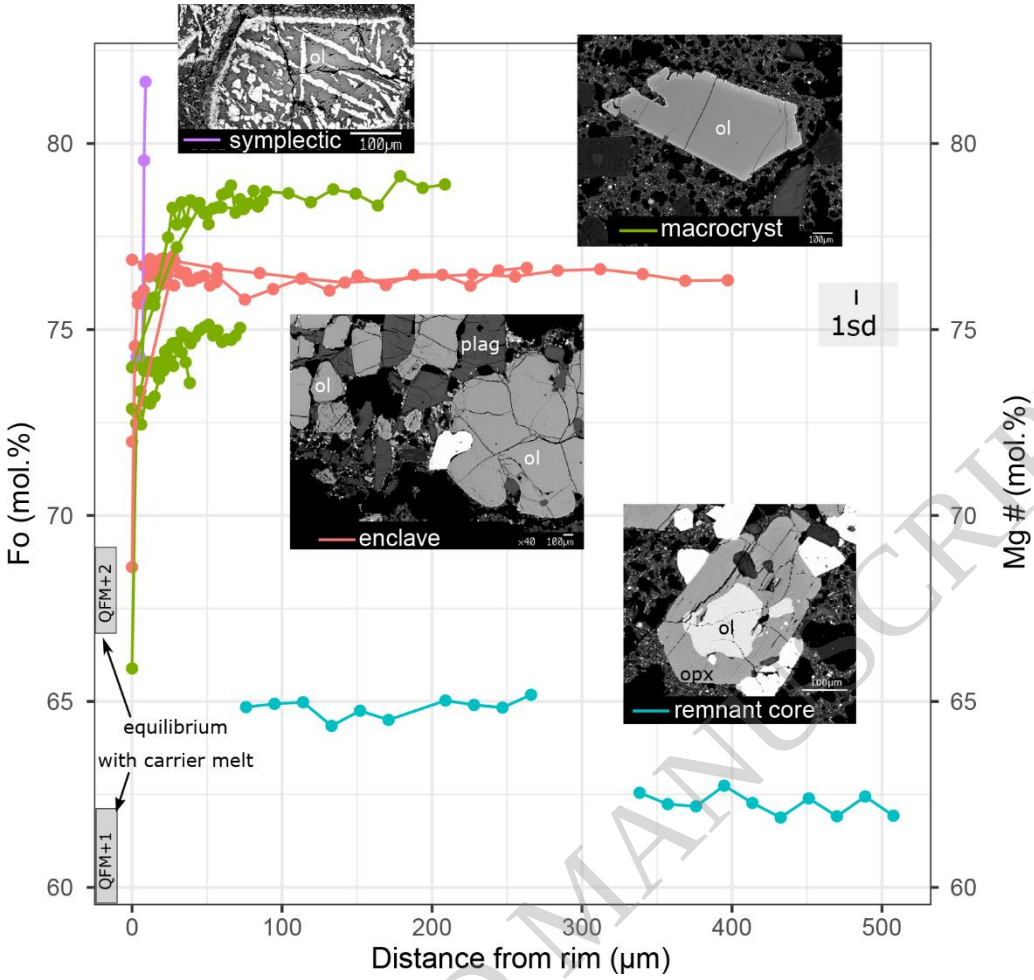

Figure 8

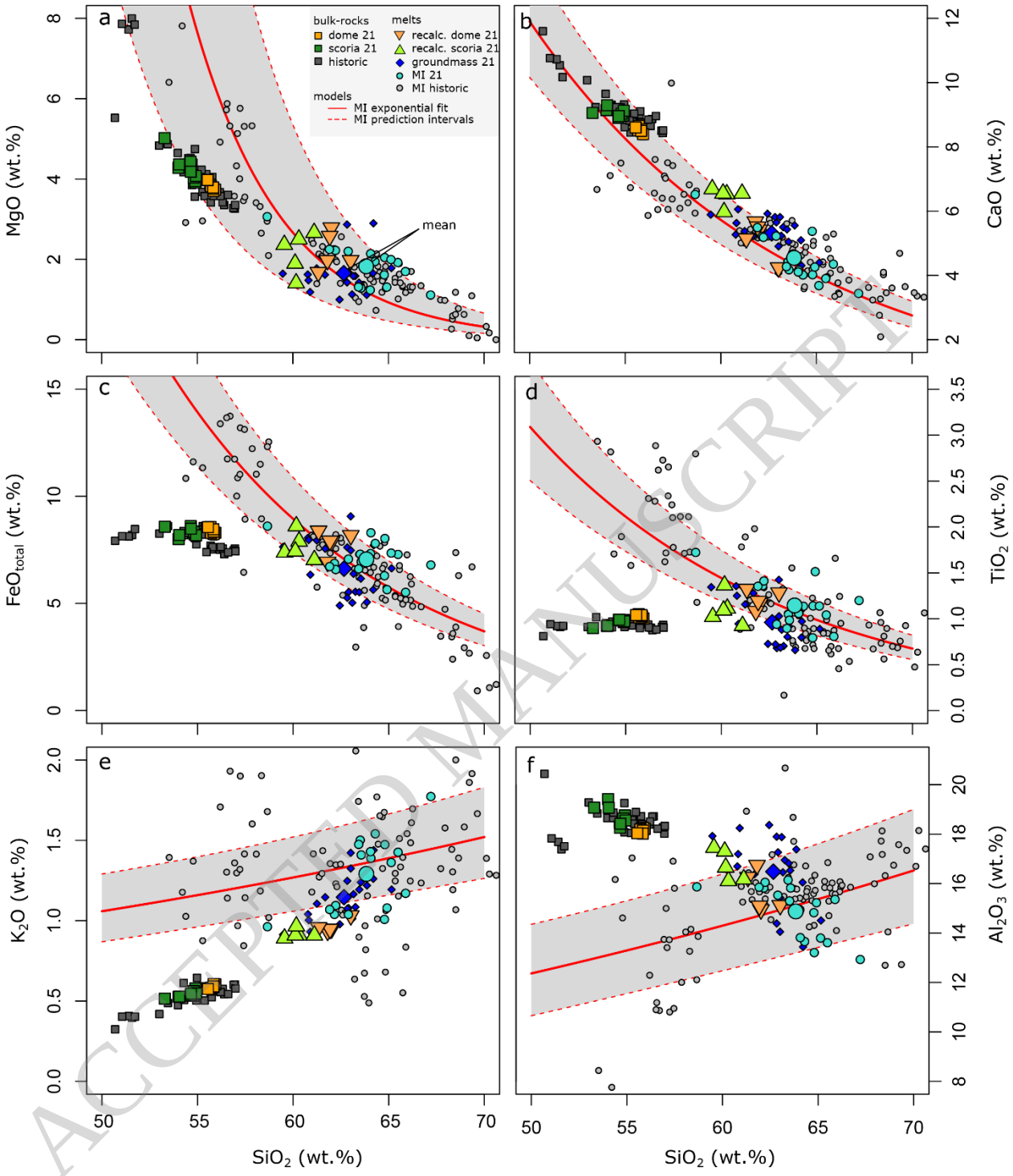

Figure 9

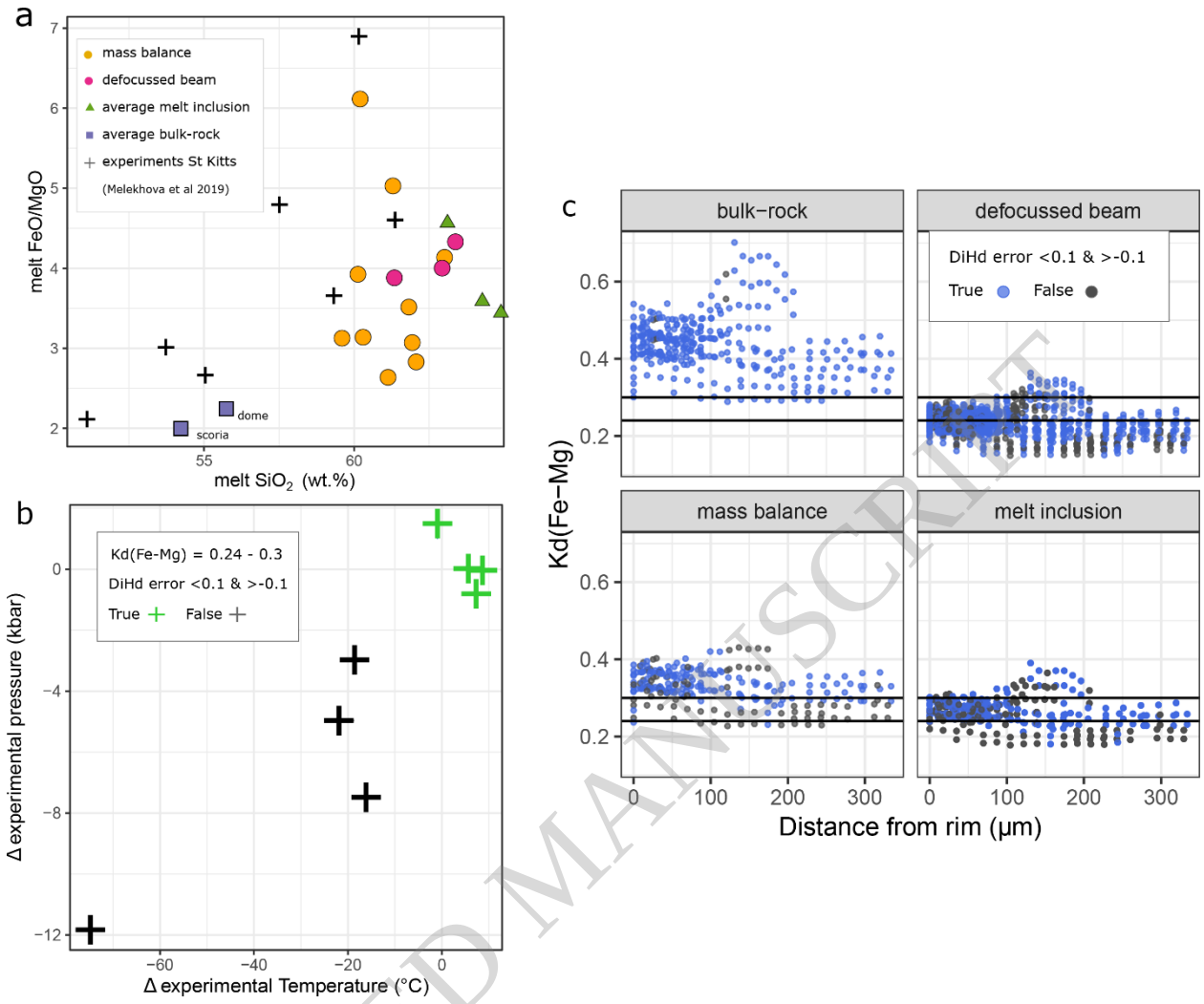

Figure 10

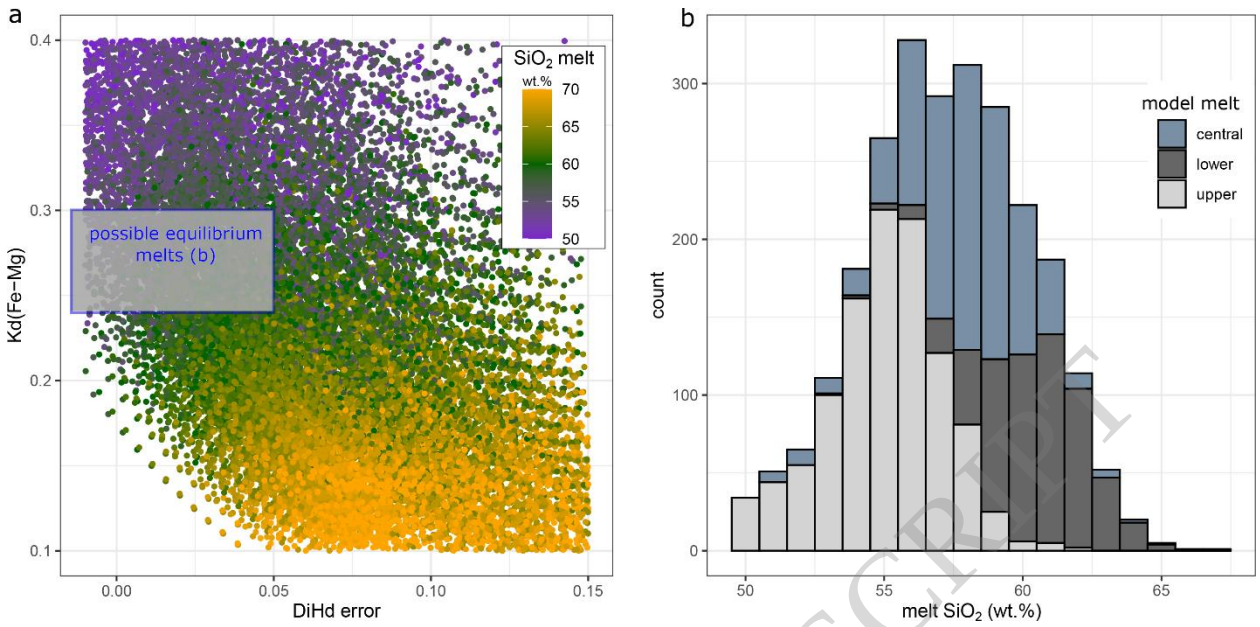

Figure 11

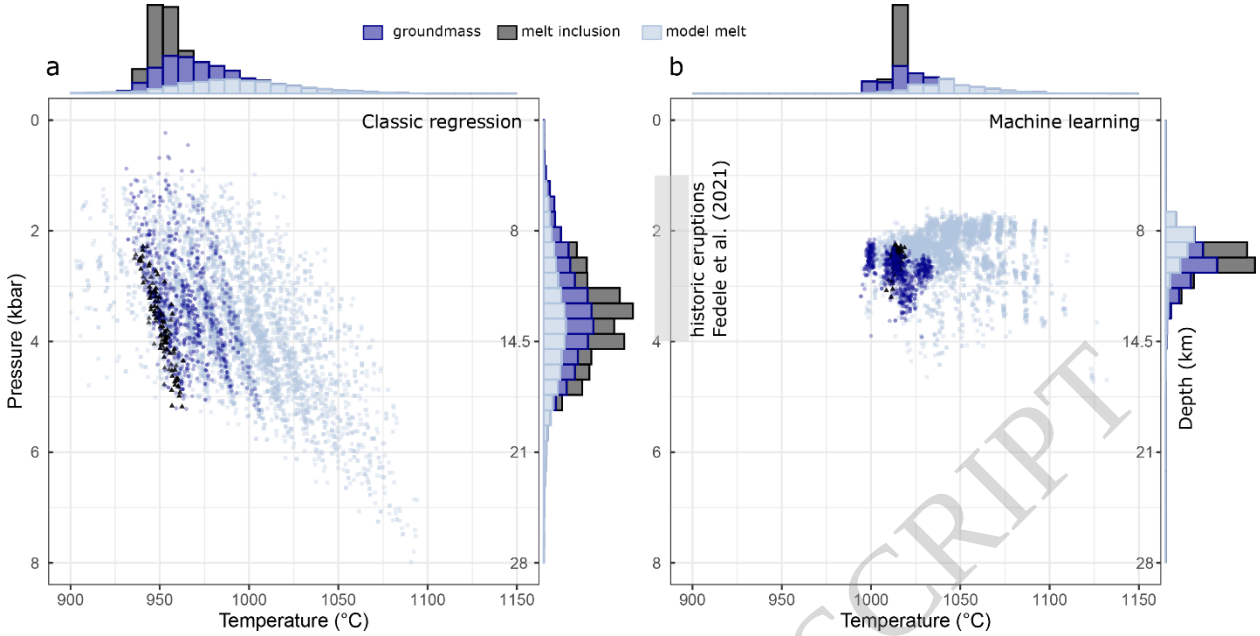

Figure 12

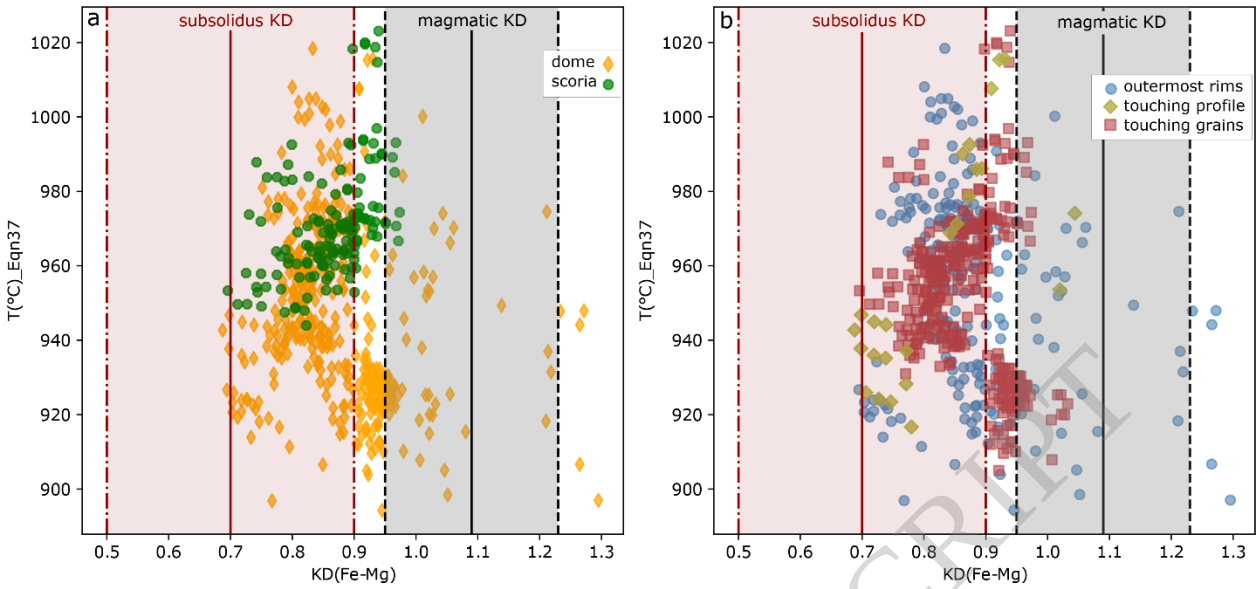

Figure 13

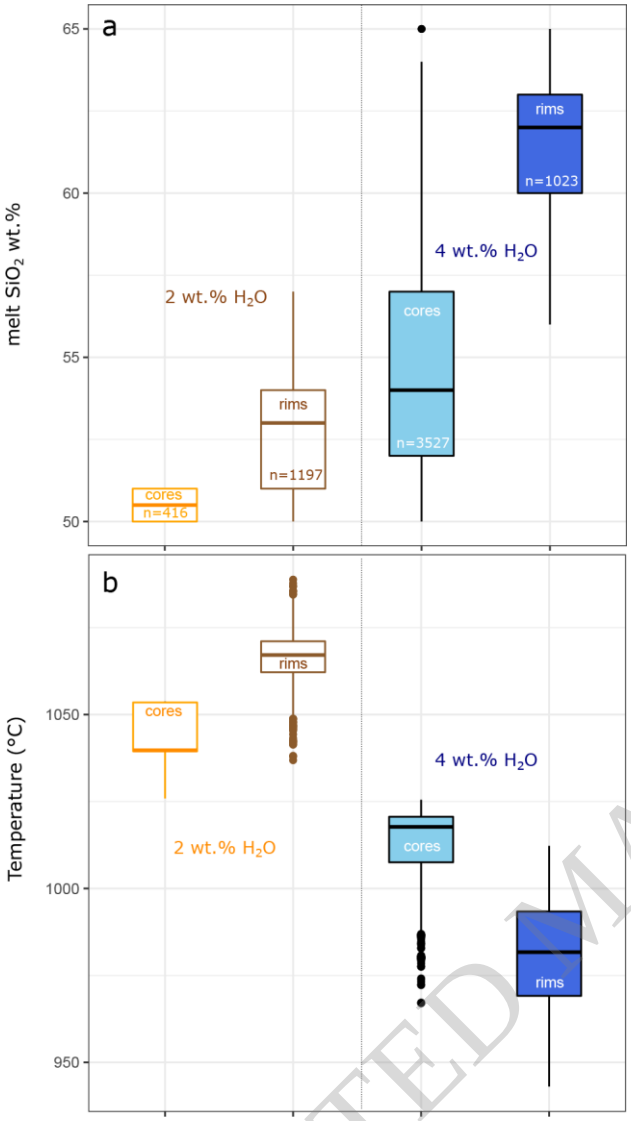

Figure 14

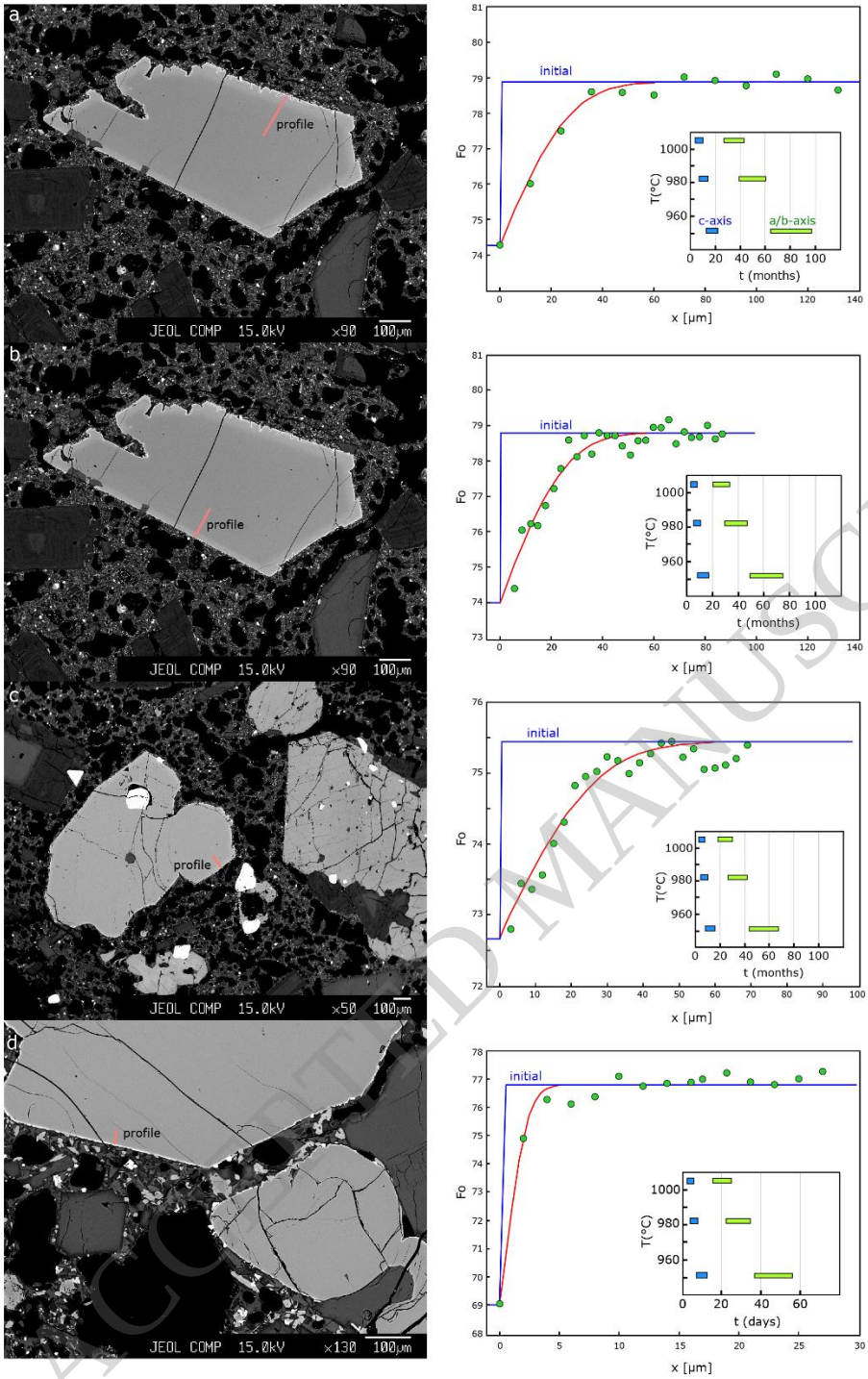

Figure 15

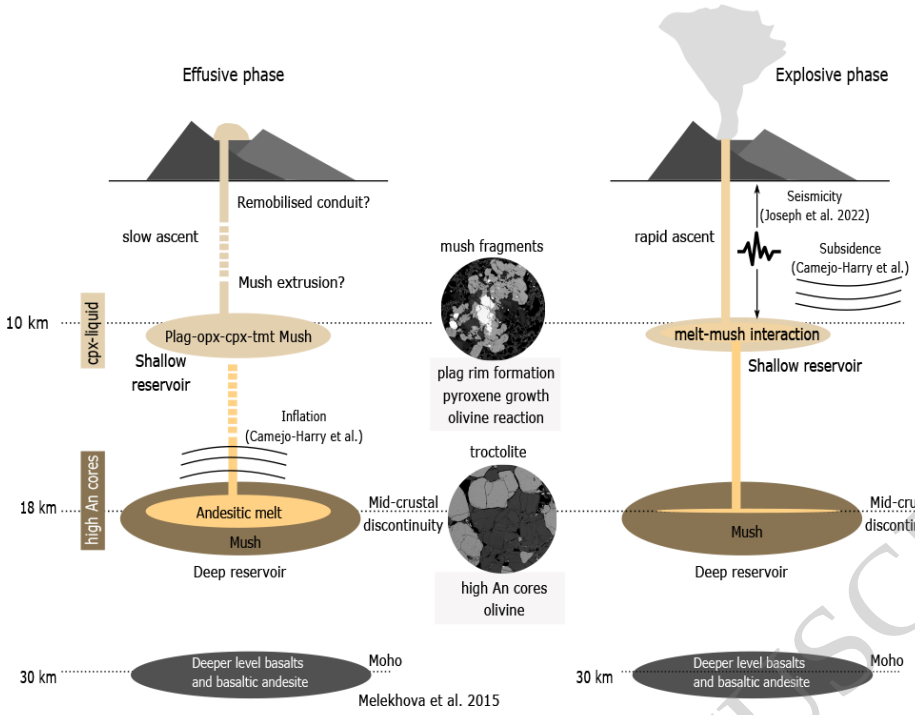

Figure 16